RSC Advances

PAPER

View Article Online
View Journal | View Issue

Cite this: *RSC Adv.*, 2022, **12**, 27648

Copper(II) complexes with 2-ethylpyridine and related hydroxyl pyridine derivatives: structural, spectroscopic, magnetic and anticancer *in vitro* studies†

Magdalena Malik, *[a] Anna Świtlicka, [b] Alina Bieńko, [c] Urszula K. Komarnicka, [c] Dariusz C. Bieńko, [a] Sandra Kozieł, [c] Agnieszka Kyzioł, [d] Tomasz Mazur[a] and Barbara Machura [b]

Copper(II) complexes with 2-ethylpyridine (**1** and **2**), 2-(hydroxyethyl)pyridine (**3**) and 2-(hydroxymethyl) pyridine (**4**) have been synthesized and characterized. All inorganic compounds have been studied by X-ray diffraction, thermogravimetry, vibrational and EPR spectroscopy as well as theoretical methods. The geometry of the complexes **1**, **3** and **4** adopts nearly perfect geometry close to square planar (**1**, **4**) or square pyramid (**3**) stereochemistry, respectively. The distortion of five coordinated copper(II) ions in complex **2** indicates intermediate geometry between square pyramidal and trigonal pyramidal geometry. Further, the magnetic measurements have shown antiferromagnetic behaviour of the prepared complexes in a wide range of temperatures. The antiferromagnetic behaviour of **2** should originate from the superexchange interactions between each copper(II) ion by the mixed chloride and μ_4-O ion pathways. Besides, the weak antiferromagnetic character of **2** can be also attributed to the presence of intrachain exchange between dimeric units through double oxide ion. In complex **3**, strong antiferromagnetic coupling between Cu(II) centres in the $Cu_2O_2Cl_2$ moiety is found. The cytotoxicity of all compounds was tested *in vitro* against various cancer cell lines: human lung adenocarcinoma (A549), human breast adenocarcinoma (MCF7), human prostate carcinoma; derived from metastatic site: brain (DU-145) and two normal cell lines: human embryonic kidney (HEK293T) and human keratinocyte (HaCat). Furthermore, Pluronic P-123 micelles loaded with selected complexes (**1** and **3**) were proposed to overcome low solubility and to minimize systemic side effects. More detailed study revealed that complex **3** loaded inside micelles causes DU-145 cells' death with simultaneous decrease of mitochondrial membrane potential and a high level of reactive oxygen species generation. The stability of the compounds **1**–**4** in DMSO was confirmed by UV-Vis and FT-IR spectra studies.

Received 16th August 2022
Accepted 21st September 2022

DOI: 10.1039/d2ra05133h

rsc.li/rsc-advances

Introduction

Several halide or mixed ligand copper, cobalt and manganese complexes of the substituted pyridine and pyridine alcohols have appeared in the literature. Some of them are mononuclear, binuclear, and polymeric complexes, which can be used as model species for active sites of biological metalloenzymes.[1–10] Several halide copper complexes with pyridine (py), including isomers as general formula: $Cu(py)_2X_2$, $Cu_2(py)_2X_4$, $Cu_4(py)_4OX_6$ and 4-methylpyridine or 2-methylpyridine (2-picoline, 2-pic): $Cu(2\text{-pic})_2Cl_2(OH_2)$, and dimeric $[Cu(2\text{-pic})_2Cl_2]_2$ coordination compounds are known.[4] Additionally, the chirality of the square planar Pt and Pd complexes with substituted pyridines ([H2etpy][$PtCl_3$(2etpy)], *trans*-[$PdCl_2$(2etpy)$_2$], *trans*-[$PdCl_2$(2-mepy)$_2$], *cis*-[PtI_2(2etpy)$_2$]; 2etpy-2ethylpyridine, 2mepy-methylpyridine) plays an important role in the interaction mechanism of these complexes with DNA.[10,11]

A wide variety of pyridine-based alcohols and their metal compounds, *i.e.* Co(II), Ni(II) complexes have been studied in the last years.[8] Furthermore, the 2-(hydroxyethyl)pyridine (Hhep) could be a good candidate to form coordination species with interesting magnetic behaviour ($[Ni(C_7H_8NO)_2(H_2O)_2](NO_3)_2$, $[Cu(C_7H_8NO)_2(SO_4)]_n$)[8] which we have decided to check for the

[a]Faculty of Chemistry, Wroclaw University of Science and Technology, Wybrzeże Wyspiańskiego 27, 50-370 Wrocław, Poland. E-mail: magdalena.malik@pwr.edu.pl
[b]Department of Crystallography, Institute of Chemistry, University of Silesia, Szkolna 9, 40-006 Katowice, Poland
[c]Faculty of Chemistry, University of Wroclaw, F. Joliot-Curie 14, 50-383 Wrocław, Poland
[d]Faculty of Chemistry, Jagiellonian University, Gronostajowa 2, 30-387 Kraków, Poland

† Electronic supplementary information (ESI) available. CCDC 2081700, 2081701, 2081702 and 2125621. For ESI and crystallographic data in CIF or other electronic format see https://doi.org/10.1039/d2ra05133h

complexes obtained by our group. Nowadays, research on the pyridine-based alcohols and their metal complexes focuses on the synthesis of the coordination monomers and polymers, which have been useful in catalysis, and modern electronics (*e.g.* OLEDs, organic light-emitting diodes) or species with magnetic properties.[8] Additionally, the ligand Hhep is an outstanding compound, which attracted attention in biology and biochemistry with practical applications, *i.e.* in the synthesis of biologically active complexes.[12–15] A great example is a gold(III) complex with 2-(hydroxyethyl)pyridine (Hhep) possessing significant anticancer activity against a human lung adenocarcinoma cell line (A549) and human breast adenocarcinoma (MCF-7).[16a] Additional study of gold(III) complexes with 2-(hydroxymethyl)pyridine (Hhmp) revealed that $[AuCl_3(Hpm)]$ and $[AuC1_2(pm)]$ complexes retain an appreciable cytotoxicity *in vitro* against the tumor cell lines T-Lymphoblastoid cell line, SKOV3 and A2780 Human Ovarian cell line and lines resistant to cisplatin[12].

The pyridine-based alcohols can form different coordination modes with metal ions, *i.e.* monodentate chelating by N-atoms, or chelating and bridging by N,O-atoms in the deprotonated form of such ligands.[6] Additionally, 2-(hydroxymethyl)pyridine and homologous alcohols have been used in manganese chemistry to obtain single molecule magnets (SMMs) type.[6] These ligands are commercially available but they have not been employed widely as popular ligands in coordination chemistry. In recent years Hhmp (2-(hydroxymethyl)pyridine, 2-pymet) has been used in copper coordination chemistry to obtain new mononuclear structures with six coordinate Cu(II) ions, where pyridine alcohol binds as a chelating ligand. There are only a few reports on the structures with the anionic hmp ligand, which can form a chelating bridging mode or the polynuclear complex.[17] In addition, structures with Hhep/hep (2-(hydroxyethyl)pyridine; 2-pyet/deprotonated one) occur less frequently. Copper(II) mononuclear complexes with Hhep have been synthesized from simple bromide and chloride (CuX_2, X = Br, Cl) in methanolic solution. Such examples are polymers $[Cu_2(\mu\text{-}Cl)_2(\mu\text{-hep})_2]_n$ (ref. 9) and $[Cu_2(hep)_2Cl_2]_n$, where the centrosymmetric dimeric units are stabilized by weak inter-dimer interactions arising from bridging Cl ligands to form a polynuclear chain with di-μ-O (from deprotonated ligand, hep) and di-μ-Cl bridges.[5] The biological properties and spectroscopic studies of copper-2-(hydroxyethyl)pyridine complexes, which we report here, have not been conducted before. Lah and coworkers synthesized others copper(II) complexes with the neutral forms of the pyridine alcohols, that have $Cu_2(OR)_2X_2$ core, *i.e.* $[Cu(2\text{-pymet})_4Cl_2]Cl_2\cdot 2H_2O$, $[Cu(2\text{-pyet})_2Br]Br$,[2] $[Cu_2(\text{-Hhmp})_2Cl_4]_n\cdot 2nCH_3OH$, and complexes with deprotonated 2-(hydroxypropyl)pyridine (hpp) $[Cu_2(hpp)_2Br_2]$, $[Cu_4(hpp)_4Br_4]$ and $[Cu_4(hpp)_4Cl_4]$.[5] The mechanism of the deprotonation pyridine-based alcohols in complexation is not clear. It is hard to explain why complexes with an alkoxide-bridge can be formed rather than with a hydroxide-bridge.[5] The search through the Cambridge crystal Database (CSD) shows some metal complexes possessing pyridine-based alcohols, *i.e.* $[Co_2(\mu\text{-}Cl)_2(mpy)_4]Cl_2\cdot 2H_2O$, $[Co(dmpy)_2]Cl_2$, $[Co(Cl)_4](Hpyet)_2$ (where mpy: 2-methanolpyridine, dmpy: 2,6-dimethanolpyridinie, hpyet: 2-ethanolpyridinium)[1] which confirms that these studies are still valid. Mobin and Mohammad obtained the monomeric ionic cobalt(II) complexes, $[Co(hep\text{-}H)(H_2O)_4](SO_4)_2$ and $[Co(hep\text{-}H)_2(H_2O)_2](NO_3)_2$ and rearranged them by heat using the SCSC (Single-Crystal-to-Single-Crystal) transformation.[7] Besides, the biological properties were not presented in the previous works.

In this paper, we report the preparation and structural characterization (X-ray analysis, FT-IR and Raman spectra, thermal studies), magnetic behaviour and biological activities of the four complexes, Cu(II) with 2-ethylpyridine (compounds **1** and **2**) and with 2-pyridineethanol (2-(hydroxyethyl)pyridine), and 2-pyridinemethanol (2-(hydroxymethyl)pyridine) complexes **3** and **4**, respectively. Most importantly, two of them (**1** and **2**) have been synthesized for the first time. Moreover, we have focused on completing the incomplete data for the previously known and poorly described Cu(II) complexes **3** and **4**. Herein we discuss and compare the obtained results for **1–4** complexes and support them with theoretical calculations.

In this work, the stability of the compounds in solution was confirmed by the results of the UV-Vis and FT-IR analysis.

An important goal of our work, following the structural characteristics, is to find the relationship between the biological activity of the synthesized complexes and the N-donor ligands used. We will also evaluate the effect of chelation in the case of hydroxyl derivatives of pyridine ligands on the presented biological properties. The results presented by us indicate the suitability of selected ligands used in the synthesis with copper(II) ions for the construction of functional materials showing magnetic and biological properties.

Results and discussion

Synthesis

The general procedure of synthesis of the four complexes is described in the experimental part and visualized in Scheme 1. The synthesis involved mixing methanolic solutions of copper(II) salts with ligands and was carried out under reflux or in the air and gives expected products. Single crystals suitable for crystallographic measurements were determined by the X-ray diffraction method.

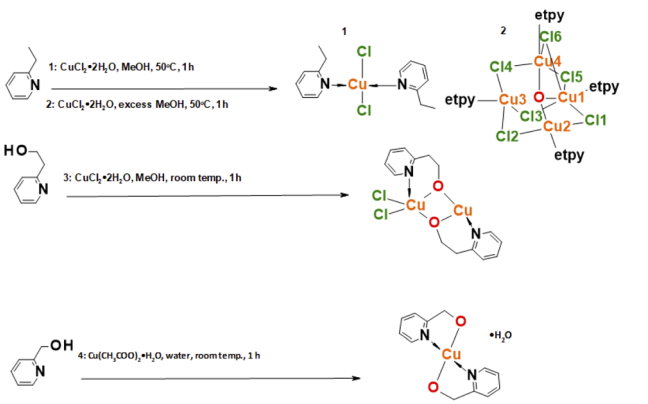

Scheme 1 Scheme of synthesis complexes **1–4**; etpy: 2-ethylpyridine.

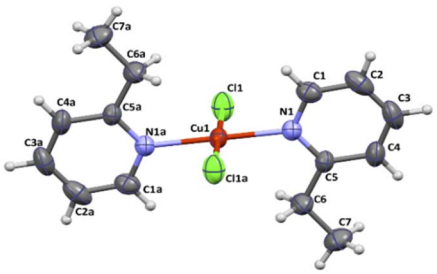

Fig. 1 Molecular structure of $[CuCl_2(etpy)_2]$ together with the atom numbering. Displacement ellipsoids are drawn at 50% probability level.

Table 1 Selected bond lengths (Å) and angles (deg) for **1**[a]

Bond lengths [Å]		Bond angles [°]	
Cu(1)–N(1)	1.9935(18)	N(1)–Cu(1)–N(1)a	180.0
Cu(1)–N(1)a	1.9935(18)	N(1)–Cu(1)–Cl(1)	89.89(5)
Cu(1)–Cl(1)	2.2524(6)	N(1)a–Cu(1)–Cl(1)	90.11(5)
Cu(1)–Cl(1)a	2.2524(6)	N(1)a–Cu(1)–Cl(1)a	89.89(5)
		Cl(1)–Cu(1)–Cl(1)a	180.00(4)

[a] Symmetry code: (a): $1-x, 1-y, 1-z$.

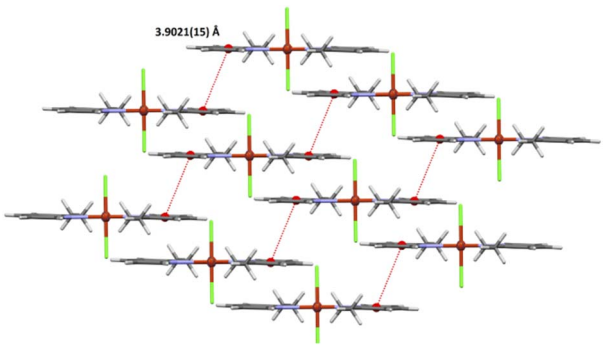

Fig. 2 A view of the crystal packing showing intermolecular π···π stacking interactions for **1**.

Crystal structures of complexes

All crystal data and structure refinement for complexes **1–4** are summarized in Table S1.†

X-Ray analysis revealed that compound **1** crystallizes in the triclinic $P\bar{1}$ space group and it is composed of neutral *trans*-$[CuCl_2(etpy)_2]$ mononuclear units, where the copper(II) ion is four-coordinate with two monodentate pyridine-based ligands and two chloride anions. The perspective view showing the molecular structure together with the atom numbering is presented in Fig. 1, while the selected bond distances and bond angles are summarized in Table 1.

In order to estimate the angular distortion from the square planar geometry of **1**, the Okuniewski's (τ'_4) parameter,[18] as well as the SHAPE program[19] based on Continuous Shape Measures (CShM) concept, were used. The shape value ($S_Q(P)$) concerning the square planar geometry was found for 0.372, while the calculated distance to the ideal tetrahedral geometry is following 33.581. The square planar geometry of metal ion is confirmed by Okuniewski parameter ($\tau_4' = 0$). The Cu–N and Cu–Cl bond distances [Cu(1)–N(1) = 1.9935(18) Å, Cu(1)–N(1) *a* = 1.9935(18) Å, Cu(1)–Cl(1) = 2.2524(6) Å, Cu(1)–Cl(1) *a* = 2.2524(6) Å; (a): $1-x, 1-y, 1-z$] are comparable with those of copper(II) compounds with the CuN_2X_2 chromophore in the same geometry.[20–23] The coper(II) ions in **1** are well separated from each other, the shortest intermolecular metal–metal distance being 7.5197(9) Å.

The crystal packing analysis[24] revealed that the molecules *trans*-$[CuCl_2(etpy)_2]$ are linked into dimers through π···π stacking with centroid-to-centroid separations of 3.9021(15) Å (Fig. 2) (Table 2). No short intermolecular interactions were observed.

The complex **2** crystallizes in the monoclinic space group $P2_1/n$ and the crystal structure consists of tetranuclear molecules $[Cu_4OCl_6(etpy)_4]$ with well-known $[Cu_4(\mu_4\text{-}O)(\mu_2\text{-}Cl)]$ core (Fig. 3). The compound **2** consists of a tetrahedron of Cu(II) atoms held together by one central μ_4-O ion and six μ_2-Cl anions. Each chloride atom spans the edge of the tetrahedron, while one etpy molecule is bound to each Cu(II) atom *via* the pyridine nitrogen atom. The $Cu_4(\mu_4\text{-}O)$ tetrahedron is slightly distorted and the Cu–O–Cu angles and Cu–O bond length vary from 105.97(9)–113.99(10)° and 1.8853(18)–1.9086(19) Å, respectively. The chloro bridges involving Cl(1), Cl(2), Cl(3), Cl(4), Cl(5) and Cl(6) atoms are slightly asymmetrical, with Cu–Cl distances ranging from 2.3199(9) to 2.6850(9) Å and six Cu–Cl–Cu bond angles from 76.48(3) to 79.50(3)° (see Table S2†).

The distortion of five coordinated copper(II) ions can be described by the structural parameter τ angular structural index

Table 3 Short intra- and intermolecular contacts in **2** (Fig. 4)

D–H···A	D–H	H···A	D···A [Å]	D–H···A [°]
C(1)–H(1)···Cl(6)	0.93	2.65	3.341(4)	131.00

Table 2 Short π···π stacking interactions in **1**[a]

Cg(I)···Cg(J)	Cg(I)···Cg(J) [Å]	α [°]	β [°]	γ [°]	Cg(I)-Perp [Å]	Cg(J)-Perp [Å]
Cg(1)···Cg(1)[b]	3.9021(15)	0	27.34	27.34	3.4661(11)	3.4661(11)

[a] α = dihedral angle between Cg(I) and Cg(J); Cg(I)-Perp = perpendicular distance of Cg(I) on ring J; Cg(J)-Perp = perpendicular distance of Cg(J) on ring I; β = angle Cg(I) → Cg(J) vector and normal to ring I; γ = angle Cg(I) → Cg(J) vector and normal to plane J; Cg(1): N(1)/C(1)/C(2)/C(3)/C(4)/C(5). [b] Symmetry code: (b): $2-x, 2-y, 1-z$.

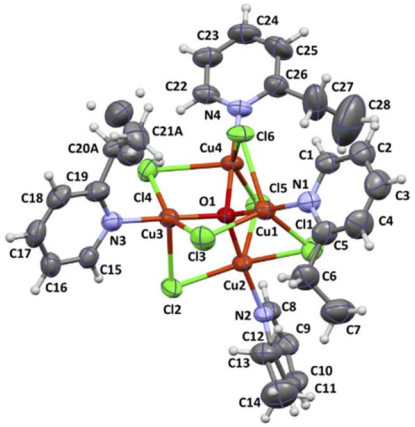

Fig. 3 Molecular structure of $[Cu_4OCl_6(etpy)_4]$ together with the atom numbering. Displacement ellipsoids are drawn at 50% probability level.

parameter τ,[25] called also the Addison parameter, it expresses the difference between the two largest angles divided by 60. Compared to the ideal values of $\tau = 1$ for a trigonal bipyramid and $\tau = 0$ for a square pyramid, the $\tau_1 = 0.77$ for Cu(1) indicates trigonal bipyramidal geometry, however structural parameters for Cu(2), Cu(3) and Cu(4) show intermediate geometry between square pyramidal and trigonal pyramidal geometry ($\tau_2 = 0.45$ for Cu(2); $\tau_3 = 0.32$ for Cu(3); $\tau_4 = 0.33$ for Cu(4)). The coordination geometries of the examined complex were also compared to two ideal geometries: bipyramidal geometry and square pyramidal using Continuous Shape Measures (CShM). The shape value concerning bipyramidal geometry was found 2.873 for Cu(1); 4.300 for Cu(2); 3.201 for Cu(3); 4.929 for Cu(4), while the calculated distances to the ideal square pyramidal are following for 5.151 Cu(1); 3.201 for Cu(2); 2.678 for Cu(3); 2.526 for Cu(4). A similar trend has been observed in literature.[26,27]

The perspective drawings of the asymmetric unit and the perspective views of 1D coordination structures of **3** are presented in Fig. 5. Their selected bond distances and angles are given in Table 4. The X-ray structure of **3** was reported previously (CCDC numbers: 611672 and 1056574) and we will refer to it only for comparison.[5,9]

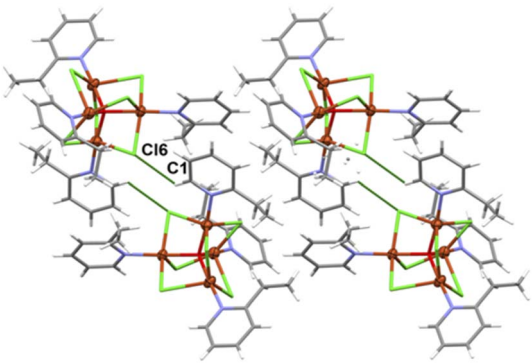

Fig. 4 Crystal packing diagram of $[Cu_4OCl_6(etpy)_4]$. The analysis of the crystal packing[24] reveals the presence of weak C–H···Cl type interactions giving rise to the formation of dimers (figure, Table 3).

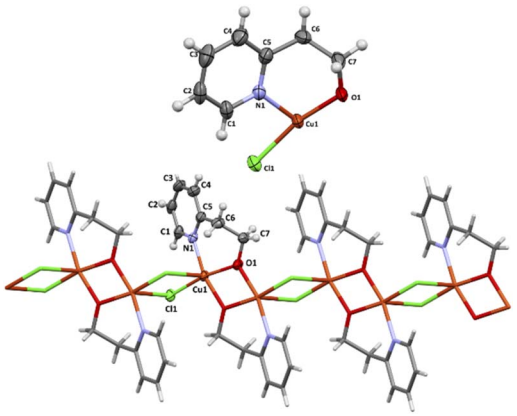

Fig. 5 The asymmetric units (top) and one-dimensional coordination chain (bottom) of **3**. Displacement ellipsoids are drawn at 50% probability.

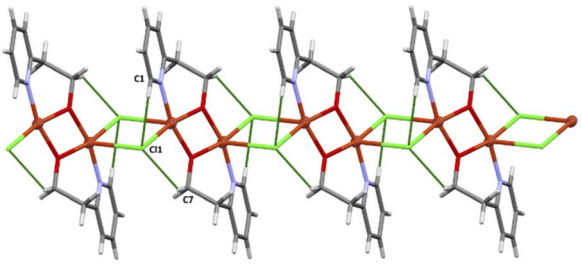

Fig. 6 Crystal packing diagram of **3**. The crystal packing analysis[24] revealed that the chains are stabilized by weak C–H···Cl interactions (see Table 5, figure).

Table 4 Selected bond lengths (Å) and angles (deg) for **3**[a]

Bond lengths [Å]		Bond angles [°]	
Cu(1)–N(1)	2.020(2)	N(1)–Cu(1)–O(1)	165.39(8)
Cu(1)–Cl(1)	2.2582(7)	N(1)–Cu(1)–O(1)c	92.79(8)
Cu(1)–Cl(1)c	2.9381(8)	N(1)–Cu(1)–Cl(1)	95.87(6)
Cu(1)–O(1)	1.9388(17)	O(1)c–Cu(1)–O(1)	74.53(8)
Cu(1)–O(1)d	1.9308(16)	O(1)–Cu(1)–Cl(1)	95.75(5)
		O(1)–Cu(1)–Cl(1)	168.08(6)
		Cu(1)–O(1)–Cu(1)d	105.47(8)

[a] Symmetry code: (c): $-x, 2-y, -z$; (d): $1-x, 2-y, -z$.

The complex **3** crystallizes in triclinic space group $P\bar{1}$ and the structure consists of neutral binuclear $[Cu_2Cl_2(pyet)_2]$ units, what results from pairing two mononuclear units related by a crystallographic centre of inversion. The dinuclear moieties are further linked through chloride bridge into one

Table 5 Short intra- and intermolecular contacts in **3** (Fig. 6)

D–H···A	D–H	H···A	D···A [Å]	D–H···A [°]
C(1)–H(1)···Cl(1)	0.93	2.62	3.205(2)	122.00
C(7)–H(7B)···Cl(1)	0.97	2.67	3.286(3)	122.00

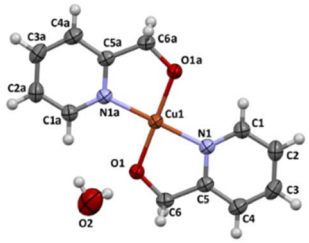

Fig. 7 Molecular structure of **4** together with the atom numbering. Displacement ellipsoids are drawn at 50% probability level.

Table 6 Selected bond lengths (Å) and angles (°) for **4**[a]

Bond lengths [Å]		Bond angles [°]	
Cu(1)–N(1)	1.982(3)	N(1)–Cu(1)–N(1)e	180.0
Cu(1)-N(1)e	1.982(3)	N(1)–Cu(1)–O(1)	84.22(9)
Cu(1)–O(1)	1.895(2)	N(1)*a*–Cu(1)–O(1)	95.78(9)
Cu(1)–O(1)e	1.895(2)	N(1)*a*–Cu(1)–O(1)e	84.22(9)
		N(1)–Cu(1)–O(1)e	95.78(9)

[a] Symmetry code: (e): $1-x, y, -z$.

dimensional structure. Each copper(II) ion is pentacoordinated by two bridging chlorides [Cu(1)–Cl(1) = 2.2582(7) Å; Cu(1)–Cl(1) *c* = 2.9381(8) Å; (c): $-x, 2-y, -z$], one pyridine nitrogen [Cu(1)–N(1) = 2.020(2) Å] and two μ–deprotonated hydroxyl oxygen [Cu(1)–O(1) = 1.9388(17) Å; Cu(1)–O(1) *d* = 1.9308(16) Å; (d): $1-x, 2-y, -z$] from pyet molecule.

The angular structural index parameter τ,[25] called also the Addison parameter, expresses the difference between the two largest angles divided by 60, and it equals 0.045. Compared to the ideal values of $\tau = 1$ for a trigonal bipyramid and $\tau = 0$ for a square pyramid, the τ values indicate geometry close to square pyramid stereochemistry. As in the previous compounds, the coordination geometry of **3** was also investigated by the continuous symmetry measures methodology[19,28,29] and the shape value ($S_Q(P)$) concerning the square pyramid geometry was found 2.829, while the calculated distances to the ideal trigonal bipyramid were following 7.444. Two types of bridges: symmetrical Cu_2O_2 and asymmetrical Cu_2Cl_2 are twisted to each other and the dihedral angles between them are 77.86(1)°. The Cu···Cu distances through Cu_2O_2 and Cu_2Cl_2 bridges as well as the shortest interchain metal···metal separation is equal to 3.0797(5), 3.8043(5) and 6.0321(6) Å, respectively.

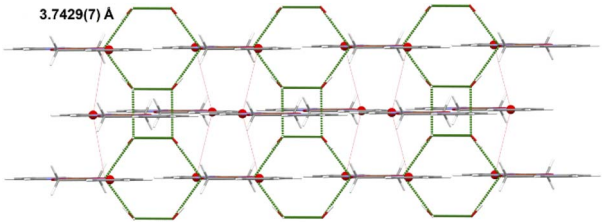

Fig. 8 A view of the crystal packing showing hydrogen bonds and π···π stacking interactions for **4**.

Table 7 Short intra-, intermolecular contacts, and π···π stacking interactions in **4**[a]

D–H···A	D–H	H···A	D···A [Å]	D–H···A [°]
O(2)–H(2A)···O(2)[f]	0.80	2.35	2.755(4)	112.00
O(2)–H(2B)···O(1)	0.80	1.92	2.753(3)	168.0

Cg(I)···Cg(J)	Cg(I)···Cg(J) [Å]	*α* [°]	*β* [°]	*γ* [°]	Cg(I)-Perp [Å]	Cg(J)-Perp [Å]
Cg(1)···Cg(1)[g]	3.7429(7)	0	16.46	16.46	−3.5895(1)	3.5895(1)

[a] Symmetry code: (f): $1-x, y, -1-z$; *α = dihedral angle between Cg(I) and Cg(J); Cg(I)-Perp = Perpendicular distance of Cg(I) on ring J; Cg(J)-Perp = perpendicular distance of Cg(J) on ring I; β = angle Cg(I) → Cg(J) vector and normal to ring I; γ = angle Cg(I) → Cg(J) vector and normal to plane J; Cg(1): N(1)/C(1)/C(2)/C(3)/C(4)/C(5), Cg(2): N(1)/C(1)/C(2)/C(3)/C(4)/C(5), Cg(3): N(1)/C(1)/C(2)/C(3)/C(4)/C(5), [&]Symmetry code: (g):$1/2-x, -1/2+y, -z$.

The X-ray structure of **4** was determined in the past (CCDC numbers: 615292, ref. 30). Complex **4** crystallizes in monoclinic *C*2/*m* space group. The perspective view of the molecular structure is shown in Fig. 7.

The copper(II) centre, coordinated to two molecules of N,O-donor ligand *via* the pyridyl nitrogen atom [Cu(1)–N(1) = 1.982(3) Å; Cu(1)–N(1)*e* = 1.982(3)Å; (e): $1-x, y, -z$] and hydroxyl oxygen atom [Cu(1)–O(1) = 1.895(2)Å; Cu(1)–O(1)*e* = 1.895(2) Å; (e): $1-x, y, -z$], adopts a distorted square planar geometry (Table 6). The shape value[19] (S_Q(P)) concerning the square planar geometry was found for 0.305, while the calculated distance to the ideal tetrahedral geometry is following 33.536. The crystal packing analysis[24] demonstrates that the molecules of **4** are linked into supramolecular 3D network by O(2)–H(2A)···O(2) [D···A distance 2.755(4) Å; D–H···A angle

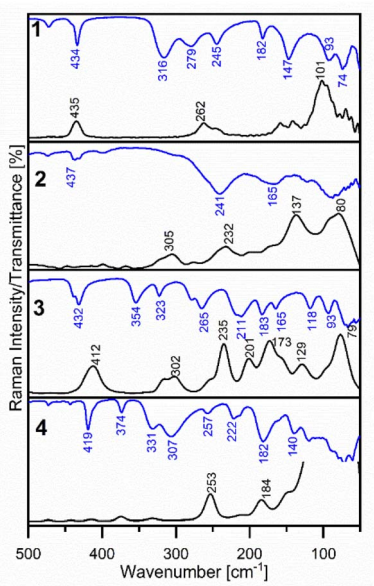

Fig. 9 The experimental frequencies of **1**–**4** complexes in FIR region.

Table 8 The characteristic metal-ligands stretching vibrations in FIR region for complexes **1–4**

	ν(Cu–N)			ν(Cu–Cl)			ν(Cu–O_L)		
	IR	Ra	Calc.	IR	Ra	Calc.	IR	Ra	Calc.
1	279m	n.o.	269	316br	n.o.[a]	336	—	—	—
	245m	ov	242	n.o.[a]	262m	260			
2	ov	305m	265[b]	241br	232br	251[b]	572s	558m	560[b]
	ov	ov	245[b]				ov	305m	305
3	280sh	ov	274	354m	ov	345	572s	545m	571
	211m, br	201m	201	265m	235s	257	323m	320sh	330
4	331s/307s	n.o.	338	—	—	—	509m	n.o.[a]	516
	257m	n.o.	276				n.o.[a]	473w	480

[a] = is observed only in IR or Raman (Ra) spectrum. [b] = averaged value of the frequency; n.o. = not observed.

112.00°] and O(2)–H(2A)···O(2)^{f} (D···A distance 2.753(3) Å; D–H···A angle 168.0°; (f): $1-x, y, -1-z$) hydrogen bonds and π–π type interactions with the centroid-to-centroid separation of 3.7429(7) Å (Fig. 8, Table 7).

FT-IR and Raman spectroscopy

The FT-IR and Raman spectra of **1–4** in the middle region are shown in Fig. S1 and S2.† Fig. 9 presents the far-infrared region of the discussed complexes absorption. A vibrational assignment of the experimental spectra was made basing on the potential energy distribution (PED) calculated by the FCART06 program using B3LYP-D3/def2-TZVP level of the theory and on the visualization in GaussView 6 program.[31]

Firstly, the spectral region from 3080 to 2817 cm^{-1} recorded in the FT-IR and Raman spectra of all synthesised complexes is characteristic of ν(C–H) stretching vibrations, however, in the IR spectra, they are presented as weak or medium bands. Next, weak bands at 1855 cm^{-1} and 1732 cm^{-1} in **1** and at 1864 and 1728 cm^{-1} in the FT-IR spectra of **2** can be assigned to overtones. The ν(C–C) and ν(C–N) stretching vibrations have generated the characteristic strong or medium bands in the 1608–1424 cm^{-1} spectral range in FT-IR spectra of **1–4**, very well predicted by theoretical calculations. Nevertheless, the N-coordination of 2-ethylpyridine, 2-(hydroxyethyl)pyridine and 2-hydroxymethylpyridine is confirmed by the presence of strong and medium bands in the frequency range 1484–1424 cm^{-1} due to ν(C=N) stretching vibrations in FT-IR spectra of the studied complexes. The medium or strong peaks in the FT-IR spectra of **1–4** at 1033 cm^{-1} (Raman: 1031 cm^{-1}), 1045 cm^{-1} (Raman: 1031 cm^{-1}), 1052 cm^{-1} (Raman: 1025 cm^{-1}) and at 1038 cm^{-1} in Raman spectra of **4**, respectively, can be assigned to the characteristic vibrations of the pyridine ring, "Star of David". The confirmation of the coordination of the 2-pyridineethanol or 2-pyridinemethanol *via* oxygen atom from –$(CH_2)_2$O– and –(CH_2)O– groups are the strong bands at 1081 cm^{-1} in the Raman spectra of **3** and at 1058 cm^{-1} in the Raman spectrum (IR: overlapped) of **4** as well. These bands are caused by stretching ν(C–O) vibrations, which have higher absorption compared to the free ligand.[16a] As it is shown in Table S3 in ESI material† the characteristic out of plane γ(C–H) bending vibrations generate the strong bands in the 999–700 cm^{-1} spectral range of the vibrational spectra of these complexes. The strong bands at 434 cm^{-1} (Raman: 435 cm^{-1}), 437 cm^{-1}, 432 cm^{-1} (Raman: 412 cm^{-1}) and 419 cm^{-1} in the FT-IR spectra of **1–4** respectively, are due to the torsion of the pyridine ring atoms (τR_{pyet}).

Fig. 9 shows the information about metal–ligand vibrations, which are found in the far infrared spectral range, below 500 cm^{-1}.

Table 8 is based on the studies of the spectra supported by theoretical calculations, which are particularly helpful in the bands assignment of the new complexes.

Besides, in complex **2** a lot of the crystal lattice vibrations coupled with the μ_4-O bridged one can be observed, and it is problematic to find copper-ligands vibrations as Nakamoto describes.[32] It is worthwhile to mention the characteristic ν(Cu–O–Cu) stretching vibrations of the atoms in μ_4-O bridge. These modes generate the medium bands at 558 cm^{-1} (calc. 560 cm^{-1}) and 305 cm^{-1} (calc. 305 cm^{-1}) in the Raman spectrum of **2**, corresponding to the antisymmetric and symmetric ν(Cu–O–Cu) stretching vibrations, respectively. To compare, in the FT-IR spectrum of **3** at 572 cm^{-1} (Raman: 545 cm^{-1}) a band assigned to the ν(Cu–O–Cu) stretching vibrations is observed as well. Furthermore, the calculated frequencies of these vibrations are in a good agreement with the experimental ones. The medium band at 412 cm^{-1} observed in the Raman spectrum of **3**, predicted by DFT calculations at 398 cm^{-1}, is due to the characteristic δ(Cu–O–Cu) bending vibrations like the "μ-O bridge breathing". In the Raman spectrum of **2** the medium peak at 305 cm^{-1} corresponding to the symmetric ν(Cu–O) stretching vibrations coupled with ν(Cu–N) can be found, in the FT-IR spectrum this band is overlapped. Additionally, the medium band at 323 cm^{-1} in the FT-IR spectrum of **3** corresponds to the ν(Cu–O) stretching vibrations. In the Raman spectrum of **4** only symmetric stretching vibration (473 cm^{-1}) is observed; antisymmetric stretching mode (ν_{as}(Cu–O)) generates only a band at 509 cm^{-1} in the FT-IR spectrum of **4**, what is expected due to the geometry of the complex **4**.

The assigned bands to the ν(Cu–Cl) stretching vibrations have higher frequencies than ν(Cu–N) stretching for complex with pyridine derivatives group. We confirm this fact in our vibrational spectroscopic study. The strong and broad peak at 316 cm^{-1} in FT-IR spectrum of **1** is due to the antisymmetric ν_{as}(Cu–Cl) stretching vibrations, where the calculated frequency is 336 cm^{-1} (100% PED). Moreover, at 262 cm^{-1} in the Raman spectrum of **1** the medium band assigned to the ν_s(Cu–Cl) stretching vibrations (60% PED) is observed, simultaneously it is not found in FT-IR spectrum, due to the square planar around the copper(II) ion in **1**. Comparing, in the FT-IR spectrum of **2** we can detect only one broad band at 241 cm^{-1} (calc. 251 cm^{-1}) and the corresponding broad peak with a maximum at 232 cm^{-1} in the Raman spectrum of complex **2**. In FT-IR spectrum of **3** there are observed two medium bands at 354 cm^{-1} and 265 cm^{-1} (Raman: 235 cm^{-1}) which can be assigned to ν(Cu–Cl) stretching vibrations. The characteristic ν(Cu–N) stretching vibrations, where N is from the pyridine ring, generate medium bands at 279 cm^{-1} and 245 cm^{-1} (in the

Table 9 Thermoanalytical data for complexes **1–4**

	DTG peak T [°C]	Temp. range [°C]	Weight loss [%] Found	Calc.	Decomposition product
complex**1**	145	128–156			
	169	156–196			
	242	196–260	61.3	61.4	$-2 \times$ 2pyet
	595	516–630	21.0	20.9	–2HCl
Total for **1**:		**128–630**	**82.3**	**82.3**	Cu as residue product
complex**2**	217	172–232	23.0	24.0	–6HCl
	241	232–240	17.0		
	581	496–632	31.0	47.0	$-4 \cdot$2etpy
Total for **2**:		**172–650**	**71.0**	**71.0**	3Cu + CuO as residue product
complex**3**	225	180–385			
	343		47.7	48.4	$-2 \times$ 2 pyet
	581	475–715	19.8	16.0	$-Cl_2$
Total for **3**:		**172–715**	**67.5**	**64.4**	$2 \times$ CuO as residue product
complex**4**	295	29–310	42		
	417	310–540	46	82	$-6H_2O + 2 \times$ 2-pyridinemethanol
Total for **4**:		**29–600**	**88**	**82**	Cu/CuO

Raman overlapped) in the FT-IR spectrum of **1**. In the Raman spectrum of **2**, the medium band at 305 cm^{-1} is found but in the FT-IR, it not be observed. The medium band at 211 cm^{-1} and shoulder at 280 cm^{-1} in the FT-IR spectrum of **3** can be assigned to the ν(Cu–N) stretching vibrations as well. The same mode generates the strong band at 307 cm^{-1} in FT-IR spectrum of **1**.

The vibrational studies confirm the results obtained by the X-ray analysis concerning the N-donor type of coordination of the 2-ethylpyridine to the Cu(II) ion in **1** and **2** and N,O-donor type of coordination of the 2-(hydroxyethyl)pyridine to Cu(II) in **3** and 2-hydroxymethylpyridine in **4**, respectively.

Stability Cu(II) complexes in DMSO solution (spectral study)

The investigation of the stability of synthesized complexes in DMSO solution was made by measuring FT-IR spectra of **1–4** after dissolving them in DSMO solvent. The spectra were measured at different intervals of time from 0–96 h and the total concentration of complexes was 2% (the FT-IR spectrum of DMSO was presented by us previously;[16a] we present selected spectra after 1 h, 24 h and 96 h).The same procedure was carried out for the stability studies of *trans*-$[PtCl_2(7AI3CAH)_2]$, *trans*-$[PdCl(7AI3CAH)_2]^+$, *cis*-$[PtCl(DMSO)(3Br4Cl7AIH)_2]^+$ and $[AuCl_3$(2-pyridineethanol)] in DMSO solution.[16a–c] In the first stage of determining the influence of DMSO on the stability of the copper(II) complexes changes in FT-IR spectrum of the solid state **1–4** comparing with these after dissolving them in a solvent were found. Immediately after dissolving Cu(II) complexes in DMSO the additional medium bands appear in FT-IR spectra; they are assigned to $\nu(CH)_{DMSO}$ stretching vibrations. Besides, the band of ν(S=O) stretching vibrations in pure DMSO recorded at 1042 cm^{-1} is shifted to the lower intensity in solutions of **1–4** (Fig S3–S8†). For this concentration of the studied complexes, it is normal to see these bands and for clarity, and to show the behavior of **1–4**, these DMSO-derived bands have not been removed. Actually, in the 1600–600 cm^{-1} spectral range the position of the bands in the IR spectra of the title complexes in DMSO remains almost unchanged in comparison to the IR spectra of **1–4** in the solid state. This fact can prove that 2-ethylpyridine, 2-pyridineethanol and 2-pyridinemethanol are not replaced by a DMSO molecule.

The medium bands at 381 and 331 cm^{-1} in the FT-IR spectrum of pure DMSO are due to scissoring $\delta(SC_2)$ and twisting $\tau(SC_2)$ vibrations, respectively. After dissolving **1–4** in DMSO solution we can observed some of them in FT-FIR spectra of the tested complexes. However, we indicate a similar position (only slight shifts are observed) of the marker bands found in the solid state complexes **1–4** compared to that in the DMSO solution.

Simultaneously, in FIR spectral region can be seen that after dissolving **2** in DMSO, it turns into complex **1**.

No new band in the 400–500 cm^{-1} spectral range which indicates $\nu(Cu–O_{DMSO})$ stretching vibrations was found.[32] It suggests that the copper(II) complexes may be stable in the used DMSO solution up to 96 hours. This investigation can give only qualitative information at that point.

Additionally, we checked the stability of synthesized complexes in DMSO/H_2O solution (9 : 1, v/v) at three different time points (0 min, 48 h and 96 h). UV-Vis spectra confirmed the stability of the complexes at room temperature (see Fig. S9†).

The studied copper(II) complexes exhibit a d–d absorption band (Fig. S9†) in 600–900 nm, in accordance with their coordination cores $\{CuN_2Cl_2\}$, $\{CuNOCl_3\}$, $\{CuNO_2Cl_2\}$ and $\{CuN_2O_2\}$ for **1–4**, respectively.[16d] The UV-Vis spectra show broader band at 855 nm (in **1** and **2**), 844 nm (**3**) and 722 nm (**4**). The higher intensity of d–d band is observed for **2** and it suggests the intermediate geometries between square pyramidal and trigonal pyramidal geometry. The visible spectra of **1** and **2** in solution are similar to each other, this indicates the environment around the copper(II) ion is the same in both complexes. Thus, complex **2**, when dissolved, turns into complex **1**. The strong absorption bands in the 200–400 nm for the complexes **1–4** are due to the $\pi \rightarrow \pi^*$ or $n \rightarrow \pi^*$ transitions;

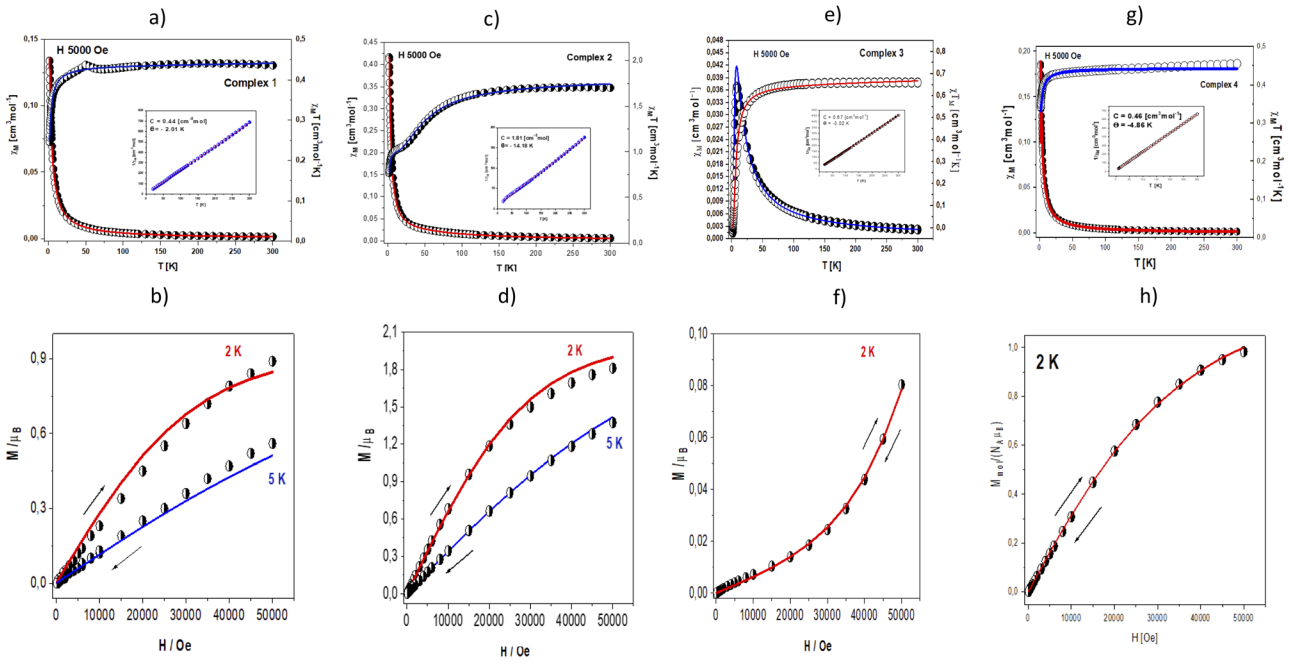

Fig. 10 Thermal dependencies of $\chi_M T$ (open circles) and χ_M (half-open circles) for (a) **1**, (c) **2**, (e) **3** and (g) **4**. The insets show thermal dependencies of inverse magnetic susceptibility. Magnetization as a function of the magnetic field for (b) **1**, (d) **2**, (f) **3** and (h) **4**. The solid lines (on all graphs) are calculated.

the strong bands at 300 nm and 313 nm (**4**) can be assigned to the ligand–metal charge transfer transitions.[16e,f]

Thermal analysis

The suggested decomposition products of **1–4** are based on mass loss calculations. Thermogravimetric, differential thermal analysis (TGA, DTGA) curves and corresponding data are illustrated in Fig. S10† and Table 9.

Complex **1** begins to decompose at 128 °C. The decomposition stage between 128 and 260 °C with three endothermic effects at 145, 169, 242 °C is related to removal of the two 2-ethylpyridine ligands with a mass loss of 61.3% (calc. 61.4%).

In the last stage of thermal decomposition **1** loses two HCl molecules from 516 to 630 °C; were found at 21.0% and calculated at 20.9%, respectively. The obtained residue product is Cu. The TG curve for **2** shows that the complex is stable up to 217 °C with the first weight loss of 23.0% (calc. 24.0%) at 172–235 °C corresponding to the loss of six Cl molecules from the coordination bridge.

In the next stages (the two endothermic peaks at 241 and 581 °C) the found value of mass loss is 48.0% due to a release of pyridine ring fragments. The successive mass loss (71.0%) may lead to Cu and CuO formation.

Complex **3** begins to decompose at 180 °C, and the decomposition stage between 180 and 385 °C with two endothermic effects at 225 °C and 343 °C is related to removal of the two 2-(hydroxyethyl)pyridine ligands with a mass loss of 47.7% (calc. 48.4%). In the last stage of decomposition **3** loses Cl_2 molecules from 475 to 715 °C; found at 19.8% and calculated at 16.0%, respectively. The obtained residue products are two molecules of CuO.

Complex **4** decomposes in two endothermic processes (the first step at 295 °C, the second at 417 °C, respectively). The assignment of these two steps involving the loss of the water molecules and the 2-pyridinemethanol ligand is problematic; therefore we suggest a residual product which can be Cu or its mixture with CuO for thermal decomposition of **4**.

Magnetic properties

Magnetic data were acquired with the help of the SQUID magnetometer (MPMS, Quantum Design) at the applied field of $B_0 = 0.5$ T and, after correction to the underlying diamagnetism, transformed to the temperature dependence of the $\chi_M T$ product (or effective magnetic moment, (Fig. 10 – top)). The field dependence of the magnetization per formula unit $M_1 = M$ mol/NA μ_B at the constant temperature is shown in Fig. 10 – below.

The χ_M values for complexes **1**, **2** and **4** increase slowly with the decrease in temperature, but in the low-temperature region, a rapid increase of molar susceptibility values occurs. Magnetic

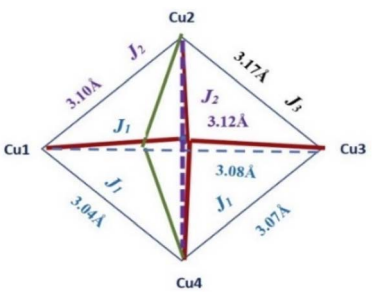

Scheme 2 A model of exchange couplings in complex **2**.

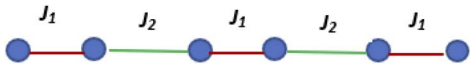

Scheme 3 Alternating Ising chain.

complex **1** and **4** present similar magnetic behaviour. The value of $\chi_M T$ at room temperature is 0.43 $cm^3\ mol^{-1}$ K (1.87 μ_B) for **1** and **4** a little bit higher than these expected for one Cu(II) ion (with $S = 1/2$ and $g_{av} = 2.00$). The $\chi_M T$ (and/or the effective magnetic moment) (Fig. 10a) decreases slowly with lowering the temperature to $T = 70$ K for 1 and 25 K for **4**. Below these temperatures, a rapid decrease of the χ_MT is registered to reach the value $\chi_M T = 0.25\ cm^3\ mol^{-1}$ K (1.40 μ_B) at 1.84 K for **1** and 0.32 $cm^3\ mol^{-1}$ K (1.61 μ_B) at 1.85 K for **4**. This feature indicates antiferromagnetic nature of the exchange interaction. The complexes obey the Curie–Weiss law in the 40–300 K temperature region (Fig. 10, inset). The fitting procedure applied to magnetic susceptibility converged to the crystal structure of examined complex. As mentioned in the structural discussion, complex **1** contains *trans*-[$CuCl_2(etpy)_2$] species which are linked into dimers through π···π stacking with the shorter Cu···Cu contact 7.489 Å. Complex **4** presents mononuclear architecture with distorted square planar geometry. In the crystal packing the molecules of **4** are linked into the supramolecular 3D network by O(2)–H(2A)···O(2) and O(2)–H(2A)···O(2) hydrogen bonds and π–π type interactions with the shortest Cu···Cu separation of 7.179 Å.

The theoretical analysis of magnetic data (Fig. 10a – line) was carried out using the PHI program,[33] what allows for the simultaneous fitting of $\chi T(T)$ and $M(H)$ dependencies. Various additional Cu···Cu intermolecular interactions transmitted through the π···π stacking are described by the effective zJ' parameter (where z is the number of adjacent paramagnetic species around a given mononuclear unit). Temperature independent paramagnetism (TIP) was also included in the fitting procedure.

The least squares fit of the experimental data by this method leads to the following results: $g_{av}(Cu) = 2.13$ and $zJ' = -0.30\ cm^{-1}$, TIP $= 75 \times 10^{-6}\ cm^3\ mol^{-1}$ for **1** and $g_{av}(Cu) = 2.15$ and $zJ' = -0.56\ cm^{-1}$, TIP $= 95 \times 10^{-6}\ cm^3\ mol^{-1}$. The discrepancy factor defined as is 3.21×10^{-5} (**1**) and 5.42×10^{-5} (**4**).

The value of the zJ' parameter suggests that the exchange interaction between the nearest Cu(II) centres in the crystal lattice in both complexes is antiferromagnetic in nature but very weak. These conclusions are also confirmed by the value of magnetization calculated per formula unit $M = M_{mol}/(N_A\mu_B)$ saturated to $M_s = 0.98\ \mu_B$ at 2 K (5 T) (1) and $M_s = 0.89\ \mu_B$ at 2 K (5 T) (**4**) (Fig. 10b and h).

In case of complex **2**, the value of $\chi_M T$ (and/or the effective magnetic moment) decreases gradually from 1.71 $cm^3\ mol^{-1}$ K (3.70 μ_B) at 300 K (a little bit higher than expected for the spin-only value for four isolated copper(II) ions with $S = \frac{1}{2}$ and $g = 2.00$) to 1.06 $cm^3\ mol^{-1}$ K (2.91 μ_B) at 20.0 K (Fig. 10c). It is typical for systems with predominantly antiferromagnetic interactions. In the temperature range of 20–5 K, a characteristic plateau observed at $\chi_M T \sim 1.05\ cm^3\ mol^{-1}$ K [$\mu_{eff} = 2.91\ \mu_B$] corresponds to the isolated ground state $S = 1$. Below 5 K, the product of $\chi_M T$ further drops down to 0.77 $cm^3\ mol^{-1}$ K [$\mu_{eff} = 2.48\ \mu_B$] at 1.8 K. It indicates the presence of additional intermolecular antiferromagnetic interactions most likely between two crystallographically independent complexes bridged by C–H···Cl type interactions (the shortest Cu···Cu distance is 7.153 Å).

The antiferromagnetic behaviour should originate from the superexchange interactions between each copper(II) ion by the mixed chloride and μ_4-O ion pathways. The fitting procedure of magnetic data of **2** (using the PHI program) was based on the quadrangle model assuming three different coupling constants, J_1 and J_2, logically corresponding to the 3 shortest Cu–Cu distances (1–3, 1–4, 3–4: J_1) 2 longest (1–2, 2–4: J_2) and one the longest (2–3) (see Scheme 2) as well as intermolecular Cu···Cu contacts described by the zJ' parameter, and the TIP parameter (Scheme 2).

The best agreement with the experimental magnetic data for **2** was obtained with $J_1 = -27.5\ cm^{-1}$, $J_2 = -14.4\ cm^{-1}$, $J_3 = -8.2\ cm^{-1}$, $g = 2.21$, $zJ' = -0.74\ cm^{-1}$ and TIP $= 61 \times 10^{-6}$ $cm^3\ mol^{-1}$, $R = \Sigma[(\chi T)\text{exp} - (\chi T)\text{calc}]^2/\Sigma[(\chi T)\text{exp}]^2 = 1.22 \times 10^{-5}$. The calculated curve matches the magnetic data well.

The magnetization per formula unit $M_1 = M_{mol}/(N_{A\mu B})$ at $B = 5$ T and $T = 2.0$ K did not reach a saturation plateau (Fig. 10d). In such a case the ground state equals $S = 2$ and the magnetization (per {Cu4} unit) should saturate to the value of $M_{sat} = 4.0$ μB. The obtained value at higher magnetic fields is much smaller indicating antiferromagnetic exchange coupling between Cu(II) ions.

In case of complex **3** molar, magnetic susceptibility shows a sharp maximum at 25 K (Fig. 10e) what is indicative of strong antiferromagnetic coupling between Cu(II) centres in the $Cu_2O_2Cl_2$ moiety.

The corresponding plot of χ_MT value (or magnetic moment) [per two Cu(II) centres] *vs.* temperature shows a decrease from 0.66 $cm^3\ mol^{-1}$ K (2.30 μB) at 300 K (lower than expected for the spin–only value for two isolated coper(II) ions with $S = \frac{1}{2}$ and $g = 2.00$) to 0.0026 $cm^3\ mol^{-1}$ K (0.14 μB) at 1.81 K.

The fitting of magnetic data of **3** was carried out using the Hamiltonian [eqn (1)] (ref. 34) for an alternating Ising chain (Scheme 3) modified by molecular field correction [eqn (2)] taking into account the two different exchange pathways, through double chloride bridge (J_1) and double oxide bridge (J_2) and the TIP parameter:

$$H = \sum_{n=1}^{N/2}\left[-2J_1 S^z_{2n-1}S^z_{2n} - 2J_2 S^z_{2n}S^z_{2n+1} - g\beta H\left(S^z_{2n-1} - S^z_{2n}\right)\right] \quad (1)$$

where $S_{2n}{}^z$ denotes the z – component of the $2n$-th spin in a linear chain

$$\chi_M = \frac{\chi_M}{1 - \frac{zJ'\chi_M}{Ng^2\beta^2}} \quad (2)$$

The zero-field susceptibility of alternating antiferromagnetic Ising chain is:

$$\chi = \frac{Ng^2\beta^2}{4KT}\left[\frac{e^{K_1+K_2}}{\cosh(K_1-K_2)}\right] \quad (3)$$

where $K_1 = \frac{J_1}{2kT}$, $K_2 = \frac{J_2}{2kT}$.

The least squares fit of the experimental data by these expressions leads to the following results: $g = 2.19$, and $J_1 = -3.71$ cm^{-1}, $J_2 = -3.08$ cm^{-1} and TIP $= 59 \times 10^{-6}$. The discrepancy factor is 7.51 10^{-5}. The variation of magnetization *versus* magnetic field at 2 K (Fig. 10f) confirms strong antiferromagnetic exchange coupling between Cu(II) ions. In such a case, the ground state equals $S = 1$, and the magnetization (per {Cu–Cu} unit) should saturate to the value of $M_{sat} = 2.0$ μ_B. The obtained value at higher magnetic fields is much smaller.

In complexes **2** and **3** the possible magnetic exchange pathways include coupling *via* double asymmetric chloro bridges and symmetric single in **2** or double **3** oxide bridge. Magnetic data clearly shows antiferromagnetic character of this interaction in both complexes (much stronger in **2**) which is in line with the data presented in the literature for similar systems. According to this, the simple magneto–structural correlations related the magnitude of exchange coupling (J) with the value of bridging angle (Cu–Cl–Cu) (φ),[4,35,36] or (Cu–O–Cu) (φ2),[36,37] and Cu–Cl/Cu–O bridge distance (R) particularly expressed by the φ/R ratio, to the more complicated factors such as geometry around the paramagnetic centres,[38–40] and angular distortions given by dihedral angle (τ) between the equatorial planes. For 98.2° values of bridging Cu–Cl–Cu angle (lower than 90°) in complex **3**, asymmetry of the chloride bridge (two different R values, one much shorter 2.258 Å and the other much longer 2.938 Å) what causes distortion of the SP geometry and an unusually long distance Cu⋯Cu (3.804 Å) a weak antiferromagnetic coupling is predicted. Additionally this fact also confirms the value of φ/R ratio equal 33.4 or 43.5, which is in agreement with the experimental results (for φ/R ratio lower than 32.6 or higher than 34.8 the exchange interaction is antiferromagnetic and for values falling in between these limits, the interactions are ferromagnetic).[41]

Finally, the weak antiferromagnetic character of **3** can also be attributed to the presence of intrachain exchange between dimeric units through double oxide ion. For dimers with planar or near planar Cu_2O_2 cores, the exchange constant (J) varies linearly with the Cu–O–Cu angle (φ). In case of **3** φ is equal to 105.5° (higher than border value of 97.5°), the interaction is predicted to be antiferromagnetic ($S = 0$ ground state). Angular distortions of LCu-O-CuL units may cause that the magnetic interaction becomes less antiferromagnetic at a given value of φ as a dihedral angle (d) between the two Cu_2O_2 planes is reduced from 180°.[42] In complex **2** the observed stronger antiferromagnetic coupling is a result of Cu⋯Cu interaction transmitted through the oxide bridge. The δ value is less than 180° as well as large Cu–O–Cu angle (from 105.97 to 111 °) spends the limit typical of such an interaction. In case of possible Cu–Cl–Cu magnetic pathway structural parameter suggested ferromagnetic properties (bridging angle from 76.9 to 79.5° lower than 90°, short Cu–Cl bridge distances from 2.332 to 2.685 Å) what is not compatible with the experimental data.

Theoretical computation

To get a more detailed view into magnetic interactions in compounds **2** and **4**, DFT calculations at the B3LYP-D3/def2-TZVP level of theory were performed to estimate the variation of spin density. The exchange coupling constants J between the paramagnetic Cu(II) ions were calculated using the "broken symmetry" approach, as implemented in ORCA. These J values were determined by taking the difference of the SCF energies calculated for the high-spin state ($S = 3/2$) and the broken-symmetry ($S = 0$) state. The BS state corresponds to configurations in which two unpaired spin-up, α electrons are localized on one site and two unpaired spin-down, β electrons are localized on the other site. The J values (using the $\hat{H} = J\hat{S}_1 \cdot \hat{S}_2$ formalism) were evaluated using the $J = 2(\varepsilon_{HS} - \varepsilon_{BS})/(\langle \widehat{S}^2 \rangle_{HS} - \langle \widehat{S}^2 \rangle_{BS})$ expression, where ε are the energies and $\langle \widehat{S}^2 \rangle$ are the average values of the total spin-squared operator in the HS and BS states.

In general, the obtained results are in line with the conclusions reached on the base of magnetic measurements.

The broken symmetry DFT calculations at the B3LYP-D3 level performed for the X-ray coordinates of the structure of **2** predicted a strongest antiferromagnetic interaction between the **1–4** ($J_1 = -18.81$ cm^{-1}), **3-4** ($J_2 = -18.64$ cm^{-1}), and **1–3** ($J_1 = -18.61$ cm^{-1}) pair of copper(II) ions and much weaker between **1-2** ($J_2 = -10.55$ cm^{-1}), **1–3** ($J_1 = -4.81$ cm^{-1}), and **2-3** ($J_1 = -3.71$ cm^{-1}). The spin densities for the high spin states are shown in Fig. S11.† The highest Mulliken spin populations are at the copper atoms (0.5744–0.5857) and oxygen atom (0.2933) while the coordinated chlorine atoms show lower spin populations up to −0.041351 (Table S4†). This suggests that a pair of magnetic orbitals, localized on the metal centres as well as on the oxygen and the magnetic superexchange interaction through the oxygen bridge is more efficient than *via* chlorine ions.

The spin density for the $\frac{1}{2}$ spin state of Cu^{II} in **3** is primarily localized on the copper ions (0.5668), but it is important to notice that this isosurface shows significant accumulation of spin density on the bridging chlorine atoms (0.1198; 0.0244) and oxygen atoms (−0.0538; −0.0351) (Table S4†). The DFT calculations showed that coupling between the Cu(II) ions should be antiferromagnetic in the nature, stronger through chlorine ions ($J_3 = -2.189$ cm^{-1}) than oxygen bridge ($J_2 = -1.783$ cm^{-1}) and this finding agrees qualitatively with the

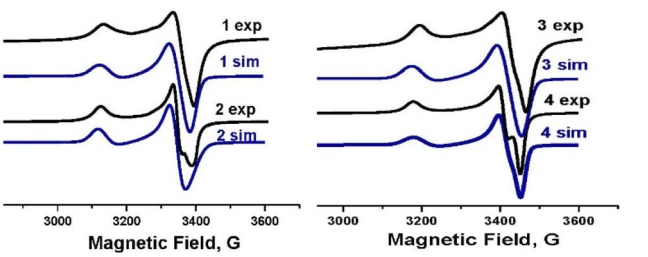

Fig. 11 The EPR spectra for **1–4** at 295 K together with the spectra simulated (1 sim–4 sim) using the parameters given in the text.

Table 10 Hydrodynamic diameter determined by DLS technique. Loading content and encapsulation efficiency for the resulting Pluronic P-123 formulations determined by ICP-MS

Formulation	Hydrodynamic diameter [nm]	LC ± SD [%]	EE ± SD [%]
Unloaded_M	19.23 ± 0.43 PDI = 0.34 ± 0.12	—	—
Complex **1M**	23.45 ± 0.46 PDI = 0.49 ± 0.11	3.97 ± 0.91	99.21 ± 0.35
Complex **3M**	23.57 ± 0.40 PDI = 0.49 ± 0.07	5.52 ± 1.84	99.41 ± 0.33

Table 11 IC_{50} [μM] for the tested compounds

	24 h				
	Non-cancerous cell lines		Cancer cell lines		
Compound	HEK293T	HaCat	MCF7	DU145	A549
Complex **1**	>1000	>1000	>1000	>1000	>1000
Complex **1M**	>1000	>1000	994.22 ± 62.6	113.05 ± 42.4	464.69 ± 31.3
Complex **2**	>1000	>1000	>1000	>1000	>1000
Complex **3**	>1000	>1000	>1000	124, 23 ± 16.20	>1000
Complex **3M**	>1000	>1000	964.21 ± 87.5	71.72 ± 13.2	615.19 ± 45.0
2-Pyridinemethanol	>1000	>1000	>1000	>1000	>1000
2-Pyridineethanol	>1000	>1000	>1000	>1000	>1000
2-Ethylpyridine	>1000	>1000	>1000	>1000	>1000
Cisplatin	21.0 ± 1.8	13.3 ± 1.1	50.9 ± 2.6	98.28 ± 1.3	56.99 ± 1.3

experimental conclusion and the coupling established within the spin model.

EPR spectra

The experimental EPR spectra of polycrystalline complexes **1–4** shown in Fig. 11 correspond to the local symmetry of Cu(II) coordination sphere close to axial and an unpaired electron in the $d_{x^2-y^2}$ orbital.

There is no change in the line shape, line width and resolution as a function of temperature.

Simulation of these spectra allowed us to determine the exact values of the g-tensor parameters $g_z = g_{\|}$, $g_x = g_y = g_{\perp}$, $g_{av} = 1/3(g_{\|} + 2g_{\perp})$ a measure of the interaction between the magnetic moment of the unpaired electron of Cu(II) ion. The smallest g−tensor anisotropy for complex **4** ($g_{\|} = 2.200$, $g_{\perp} = 2.052$ and $g_{av} = 2.101$) corresponds to the planar geometry of the anion with averaged cis–angle of 90° what is only the third known example with square planar geometry examined by EPR.[43]

In case of the rest of examined complexes the values of the g-tensor are higher: ($g_{\|} = 2.209$, $g_{\perp} = 2.059$ and $g_{av} = 2.109$) for **1**, ($g_{\|} = 2.212$, $g_{\perp} = 2.062$ and $g_{av} = 2.112$) for **2** and ($g_{\|} = 2.214$, $g_{\perp} = 2.058$ and $g_{av} = 2.111$) for **3** due to the change of geometry from planar to trigonal pyramidal.

Biological properties

Complex **4** turned out to be very toxic towards healthy cells and inactive against cancer cells so only **1** and **3** compounds, nontoxic towards normal cells, were encapsulated into polymeric micelles made of Pluronic P-123 (PEO-PPO-PEO triblock copolymer), using thin-film hydration method (Table 10 and 11).[44] Complex **2** after being dissolved in biological medium adopts the same structure as compound **1**, what was confirmed by UV-Vis spectra and FT-IR spectroscopy.

Zeta potential of stable Complex **1M** and Complex **3M** micelles was determined to be −1.83 ± 0.23 mV and −1.67 ± 0.33 mV (pH = 7.4), respectively. This slightly negative potential results from the uncharged PEO amphiphilic copolymers and it is in agreement with our previous results[44] and also these of other researchers.[45]

Cytotoxicity of the copper(II) complexes (**1**, **2**, **3**), starting ligands (2-pyridineethanol, 2-pyridinemethanol, 2-ethylpyridine) and nanoformulations of Cu(II) complexes (complex

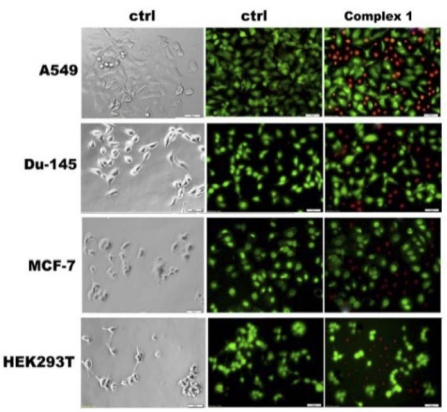

Fig. 12 Selected images of cancer cells treated with complex 1_M in IC_{50} (magnification 20.00×, bar 50 μm). The green cells with normal morphology are viable ones (fluorescein diacetate, FDA), while round red cells are dead (propidium iodide, PI).

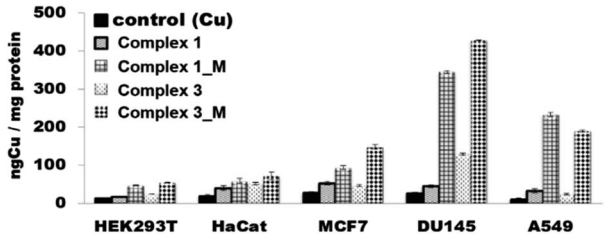

Fig. 13 Time-dependency of final intracellular copper concentration expressed as ng Cu per mg protein after 24 h of incubation with the HEK293T, HaCat, MCF7, DU145 and A549 cell lines for **1** and **3** complexes in $c = 1$ μM.

1M, complex **3M**) was tested *in vitro* against various cancer cell lines: human lung adenocarcinoma (A549), human breast adenocarcinoma (MCF7), human prostate carcinoma; derived from metastatic site: brain (DU-145). Additionally, complexes **1**–**3** and starting ligands were tested towards two immortalized human embryonic kidney (HEK293T) and human keratinocyte (HaCat) cell lines. The results of this assay are shown in Table 11 together with the results obtained for cisplatin (the reference drug). We have chosen these types of the cells to our investigation because recently published statistics have shown that for the past two decades lung, breast and prostate cancer – are the most common cancer types.[46]

As shown in Table 11, neither the ligand itself or the complexes **1** and **2** displayed significant cytotoxicity towards all the tested cancer cell lines in concentration below 1000 μM.

All complexes contain copper ion, however, only **3** exhibits activity toward DU-145 cancer cells whereas **1** and **2** are inactive, what suggests that the chelating ligand also plays a role. The enhanced anticancer activity of complex **3** may result from the introduction of two 2-pyridineethanol molecules, with additional –OH moiety compared to the second ligand, which, as indicated by the results of the experiments described in the next section, increased intracellular copper concentration in cancer cells. It is noteworthy that the two tested copper(II) complexes (**1** and **3**) did not exhibit toxicity toward HEK293T and HaCat normal cell lines in opposition to **4** which turned out to be highly toxic. Therefore, this compound (**4**) was not subject to further biological research. In general, the cytotoxicity of the synthesized complex **3** against the human cancer cell lines exhibits similar activity as observed in analogous copper-based complexes.[47–49a] For example, comparable observations were made by Andrew Kellett *et al.*[47] who prepared Cu(II) complexes with several derivatives; one of the copper complexes was active, while the corresponding ligands were not in 24 h of incubation. Results from this study are similar to our data in that there was a significant variation in the activity of the different compounds towards human cells. Obviously, several copper(II) complexes with much better cytotoxicity against cancer cells have already appeared in the literature.[49b,c]

The use of liposomal or polymeric formulations loaded with chemotherapeutics significantly increases the therapeutic index of many drugs, and provides the intended drug targeting and controlled release.[50,51] To enhance anticancer properties of metal complexes and to control their uptake only by tumor cells over the normal ones, we encapsulated metal compounds into Pluronic P-123 micelles. Of note, the determined IC_{50} values for complex **1M** and complex **3M** are one order of magnitude lower than these in case of the corresponding complexes studied in solution for A549 and MCF7 cells, while, in case of the most sensitive line (DU-145), this activity was about 10 times lower for complex **1M**. In terms of new drugs development for human use, this information is quite important for the safe and effective use to obtain the desired clinical effect.

To confirm the determined cytotoxicity, viable and dead cells were survival stained with fluorescein diacetate (FDA) and propidium iodide (PI) after treatment, and the effect was visualized under a fluorescence microscope (Fig. 12). FDA was used as a versatile fluorescent dye in the form of a cell-permanent esterase substrate. Only in viable cells with suitable enzymatic activity fluorescein is intracellularly generated and serves as a viability probe, while PI was applied as a red-fluorescent cell viability dye, which is excluded from live cells with intact membranes, but penetrates dead or damaged cells and binds to DNA and RNA by intercalating between the bases.

Searching to correlate the cytotoxic activity of the complexes with their ability to enter the cells, the quantitative assessment of the uptake of the compounds in cells was performed by determining their total Cu content using ICP-MS. The delivery of copper into cells is hampered by several specific and non-specific proteins which block theirs entrance. However, once entering the cells copper complexes are capable of inducing apoptosis.[52] A comparison of the cytotoxicity data depicted in Table 11 and the cellular uptake data presented in Fig. 13 indicates that the antiproliferative effects of the complexes were slightly more pronounced in DU-145 cells than in others cells (HaCat, HEK293T, A549, MCF7). As it can be evinced from the data reported in Fig. 13, under the same conditions in DU-145

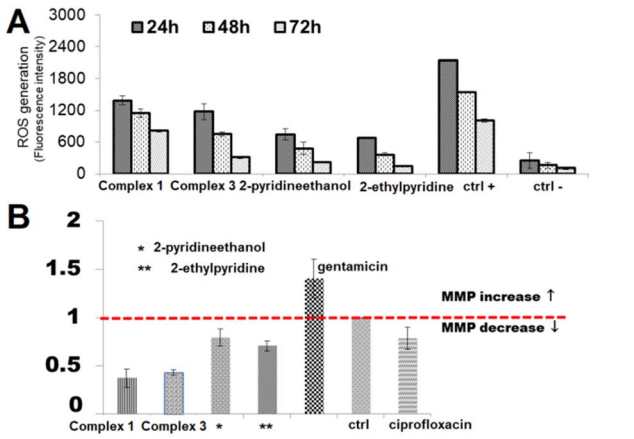

Fig. 14 (A) The ROS generation monitored by H_2DCF-DA assay in DU-145 cells during steady incubation with complexes and their corresponding ligands for 24, 48 and 72 h in $c = 1$ μM. ctrl(+): H_2O_2 as positive control and ctrl(−): negative control, cell without compound. (B) Influence of studied compounds (IC_{50}) on intensity of JC-10 fluorescence in treated DU-145 cells. Alteration in MMP is given as an emission ratio 570 nm/530 nm. (ctrl – untreated cells, ciprofloxacin – a negative control, gentamicin – a positive control).

cells, the cellular uptake of complex **1M** and complex **3M** was greater than non-encapsulated complexes. The fact that compounds can easily enter and accumulate inside cells is very important because cellular uptake is a crucial feature for drug effectiveness.

The generation of reactive oxygen species (ROS) has been cited as a major contributory factor to the high toxicity and anticancer activity of numerous copper complexes.

In addition, tumors and normal cells have many different features, *e.g.* cancer cells are less resistant to oxidative stress than healthy cells and therefore reactive oxygen species (ROS) can be an effective anti-tumor modality and therapeutic target for treating malignancies. They can be produced in physiological processes occurring in the cells or generated as a result of external factors such as drugs, ultraviolet, ionizing radiation or metal ions and complexes.[51,53] Therefore, to give insights into the possible mode of action of the ability of complexes (**1** and **3**) and their ligands (2-pyridineethanol, 2-ethylpyridine) to generate reactive oxygen species were studied. ROS generation was detected with the application of a nonfluorescent 2′,7′-dichlorodihydrofluorescein diacetate (H_2DCF-DA) probe as a ROS detector and monitored by fluorescence spectroscopy. The obtained results, presented in Fig. 14A, were related to the fluorescence intensity of positive control cells (K(+); in the presence of extra H_2O_2) and negative control (K(−); control untreated cells).

All compounds resulted in the production of the amount of ROS compared to negative control in the order complex **1** > complex **3** > 2-pyridineethanol > 2-ethylpyridyne. Of note, the studied complexes induced ROS generation at a significantly higher level than their uncoordinated ligands. The increase in ROS started as early as 24 h after treatment and was detectable throughout the treatment at all-time points tested (24, 48, 72 h). Hence, it appears that the Cu-complexes under investigation may induce oxidative stress in cells. It could be generalized that cytotoxicity of the present complexes is mediated by or due to ROS.

Mitochondrial dysfunction (loss of mitochondrial potential) mainly during oxidative phosphorylation and the antioxidant GSH depletion is one of the major sources of ROS-mediated cell injury in cancer. Changes in mitochondrial membrane potential ($\Delta\Psi m$) allow the evaluation of the mitochondrial function.[51,54] Breakdown of the mitochondrial membrane potential is associated with the opening of the permeability of the membrane transition pores, and release of Cyt-C, Apaf (which can combine with caspase-9 in the cytoplasm) from mitochondria. This interaction usually triggers a cascade of executive caspases (especially caspase 3 responsible for apoptotic cell death).[50]

Herein, to designate the significance of mitochondrial disorder in ROS production and finally cancer cell death induced by Cu(II) complexes, the variation in the mitochondrial membrane potential (MMP) was monitored using the JC-10 probe (Fig. 14B). Gentamicin, which causes an increase in MMP and ciprofloxacin with its opposite effect on MMP were used as a positive and a negative control, respectively.

In the present study, the decreases in mitochondrial membrane potential were found in complexes and ligands treated cells, which further indicated disruption of mitochondrial membrane integrity. Of all tested compounds, MPM is the most significantly reduced by the starting ligands (2-pyridineethanol, 2-ethylpyridine), while the least effect is caused by the copper complexes (**1** and **3**) – this trend is opposite to that of ROS generation. Thus, our foregone conclusion can be extended, that the ROS generation and the resulting cell death do not depend on the depletion of MMP.

Conclusions

In this work four copper(II) complexes with 2-ethylpyridine (**1** and **2**) and with pyridine alcohols (**3** and **4**) have been synthesized and characterized by X-ray analysis, vibrational spectroscopy, thermal analysis. Magnetic properties have been presented as well. All structural studies have been supported by theoretical computations at the B3LYP level of theory. The structure of square planar geometry **1** is composed of neutral *trans*-[$CuCl_2(etpy)_2$] mononuclear units, where the copper(II) ion is four-coordinate with two monodentate pyridine-based ligands and two chloride anions. Complex **2** crystallizes in the monoclinic space group $P2_1/n$ and the crystal structure consists of tetranuclear molecules [$Cu_4OCl_6(etpy)_4$] with well-known [$Cu_4(\mu_4\text{-O})(\mu_2\text{-Cl})$] core. The Addison parameter calculated in **3** and **4** confirms the distorted square planar geometry of Cu^{2+} ion. The vibrational study confirms the results of the X-ray analysis concerning the N-donor type of coordination of the 2-ethylpyridine to the Cu(II) ion in **1** and **2** and N,O-donor type of coordination of the 2-(hydroxyethyl)pyridine to the Cu(II) in **3** and 2-hydroxymethylpyridine in **4**, respectively. The EPR spectra confirm the local symmetry of Cu(II) coordination sphere close to the axial and an unpaired electron in the $d_{x^2-y^2}$ orbital. The thermal analysis describes the stability of these complexes and we suggest the copper or copper oxide as the residue product after decomposition **1–4**. The qualitative investigation of the stability of copper(II) complexes in DMSO solution by measuring UV-Vis and FT-IR spectra of **1–4** after dissolving them in the DSMO solvent was performed. We indicate a similar position of the marker bands found in the solid state complexes **1–4** compared to that in the DMSO solution. Moreover, no new band in the IR spectrum which will prove the replacement of already existing ligands by coordinated DMSO molecule was observed. Consequently, the Cu(II) complexes are stable in the used DMSO solution for 96 hours, which has been examined qualitatively (UV-Vis and FT-IR). The antiferromagnetic behaviour of Cu(II) complexes is shown and the interesting superexchange interactions between each copper(II) ion by the mixed chloride and μ_4-O ion pathways in **2** were indicated. In addition, cytotoxicity of all complexes was determined. Complex **2** after being dissolved in a biological medium turns to compound **1**, therefore the cytotoxicity of **2** is the same as **1**. Compound **3** exhibits moderate activity toward DU-145 cancer cells (human prostate carcinoma) whereas **1** and **2** are inactive, which suggests that the chelating ligand also plays a role. Noteworthy the two tested copper(II) complexes (**1** and **3**) did not exhibit toxicity toward

HEK293T and HaCat normal cell lines. Two (**1** and **3**) out of four titled complexes were encapsulated into polymeric micelles made of Pluronic P-123, using thin-film hydration method, and their cytotoxicity was tested *in vitro* against various cancer cell lines. After this procedure, the determined IC_{50} values for complex **1** and **3** are one order of magnitude lower than these in non-encapsulated, and most importantly in the case of the most sensitive line (DU-145), this activity was about 10 times lower for **1**. It could be generalized that cytotoxicity of the presented complexes is mediated by ROS, and the resulting cell death depends on the depletion of MMP. However further, more detailed investigations allowing to understand complete mode of theirs action are needed.

Experimental methods

General procedures

$CuCl_2 \cdot 2H_2O$, $Cu(CH_3COO)_2 \cdot H_2O$, 2-ethylpyridine, 2-pyridineethanol and 2-pyridinemethanol were purchased from Sigma-Aldrich, solvents from Avantor (POCH S.A). All reagents were used without further purification.

Preparation of copper(II) complexes, *trans*-[$CuCl_2$(etpy)$_2$] and [Cu_4OCl_6(etpy)$_4$] (1 and 2). $CuCl_2 \cdot 2H_2O$ (0.1707 g, 1.00 mmol) was dissolved in 10 mL of methanol (complex **1**) or in the excess solvent for complex **2** (min. 20 mL). The synthesis was conducted at 50 °C in both cases. To the stirred mixtures, 2-ethylpyridine (230 μl, 2.00 mmol) was added. Immediately after adding, the solution change colour from light green to deeper green in both cases. The stirring was continued for next 60 minutes. The resulting violet, large crystals (complex **1**) were obtained after 5 days; the dark green small crystals of complex **2** were noticed two days after synthesis. The crystals of complexes **1** and **2** were collected by filtration, washed with methanol and diethyl ether. The next step was the process of air drying of the crystals.

(**1**):*trans*-[$CuCl_2$(etpy)$_2$] yield: 0.1325 g, 0.380 mmol (38.0% based on $CuCl_2 \cdot 2H_2O$).

Anal. calcd for **1** (348.75 g mol^{-1}): C, 48.21; H, 5.20; N, 8.03 [%] found: C, 47.82; H, 5.06; N, 8.12 [%].

(**2**): [Cu_4OCl_6(etpy)$_4$] yield: 0.2275 g, 0.250 mmol (25.0% based on $CuCl_2 \cdot 2H_2O$)

Anal. calcd for **2** (911.51 g mol^{-1}): C, 36.89; H, 3.98; N, 6.15 [%] found: C, 37.34; H, 3.96; N, 6.01 [%].

Preparation of copper(II) complex [Cu_2Cl_2(pyet)$_2$](3). $CuCl_2 \cdot 2H_2O$ (0.1707 g, 1.00 mmol) was dissolved in 8 mL of methanol at room temperature. To the stirred mixtures, 2-pyridineethanol (226 μl, 2.00 mmol) was added. Immediately after adding, a light green precipitate was obtained. The stirring continued for next 60 minutes. The resulting green precipitate was collected by filtration, washed with methanol and diethyl ether and dried in air. The filtrate was kept for observation; purple crystals appeared from it after a week. The next step was the process of air drying of the crystals.

[Cu_2Cl_2(pyet)$_2$] yield: 0.1575 g, 0.356 mmol (35.6% based on $CuCl_2 \cdot 2H_2O$).

Anal. calcd for **3** (442.29 g mol^{-1}): C, 38.02; H, 3.65; N, 6.33 [%] found: C, 37.95; H, 3.80; N, 6.15 [%].

Preparation of copper(II) complex,[Cu(pymet)$_2 \cdot H_2O$](4). $Cu(CH_3COO)_2 \cdot H_2O$ (0.1197 g, 0.500 mmol) was dissolved in water (15.00 mL) at room temperature. To the stirred mixture, 2-pyridinemethanol (193 μl, 1.00 mmol) was added. Immediately after adding, the solution change colour to dark blue, and the stirring was continued for next 60 minutes. The resulting blue crystals were obtained after 10 weeks and collected by filtration, washed with CH_2Cl_2 and diethyl ether. The next step was the process of air drying of the crystals.

$C_{12}H_{12}CuN_2O_2 \cdot (4H_2O)$ Yield: 0.0563 g, 0.16 mmol (32% based on $Cu(CH_3COO)_2 \cdot H_2O$).

Anal. calcd for **4** (351.84 g mol^{-1}): C, 40.96; H, 5.73; N, 7.96 [%] found: C, 40.43; H, 5.58; N, 7.80 [%].

Elemental analysis was performed on a FLASH 2000 CHNS Analyzer.

Electronic absorption spectroscopy was carried out with an UV-Vis spectrophotometer (Agilent Technologies, Cary300 UV-Vis).

In order to record the UV-Vis spectra the complexes were dissolved in DMSO/H_2O (9 : 1, v/v) and measured in the intervals 0 (after dissolving), 48 and 96 h. The concentration of compounds was 10^{-6} M to record the whole range, and 10^{-4} M to record d–d bands, respectively.

Characterization of copper(II) complexes

X-ray analysis. Single crystal X-ray diffraction data of **1–4** were collected on a Gemini A Ultra diffractometer equipped with Atlas CCD detector and graphite monochromated MoKα radiation (α = 0.71073 Å) at room temperature. The unit cell determination and data integration were carried out using the CrysAlis package of Oxford Diffraction. [Oxford Diffraction, CrysAlis PRO, Oxford Diffraction Ltd, Yarnton, England, 2011]. The structures were solved by direct methods using SHELXS and refined by full-matrix least-squares on F^2 using SHELXL-2014.[55] All non–hydrogen atoms were refined anisotropically. The hydrogen atoms were placed in calculated positions refined using idealized geometries (riding model) and assigned fixed isotropic displacement parameters, d(C–H) = 0.93 Å, U_{iso}(H) = 1.2 U_{eq}(C) (for aromatic); and d(C–H) = 0.96 Å, U_{iso}(H) = 1.5 U_{eq}(C) (for methyl). The methyl groups were allowed to rotate around their local threefold axis. Details of the crystallographic data collection, structural determination, and refinement for **1–4** are given in Table S1.†

The crystal structures have been deposited at the Cambridge Crystallographic Data Centre and allocated the deposition numbers CCDC 2081700 (**1**), 2081701 (**2**), 2081702 (**3**), 2125621 (**4**).

Vibrational spectroscopy. ATR FT-IR spectra of Cu(II) complexes, 2-pyridineethanol, 2-pyridinemethanol, 2-ethylpyridine and $Cu(CH_3COO)_2 \cdot H_2O$, $CuCl_2 \cdot 2H_2O$ were collected using a Bruker Vertex 70v Fourier transform infrared spectrophotometer equipped with an air cooled DTGS detector and diamond attenuated total reflection infrared cell at 2 cm^{-1} resolution and 128 scans (for ligands only 16 scans) in the middle-infrared (4000–400 cm^{-1}) and far-infrared (600–100 cm^{-1}) regions at room temperature.

The ATR spectra of 2% solutions of copper(II) complexes in DMSO, which were obtained by dissolving 10 mg complexes in 500 mL DMSO, were measured in the intervals 1, 24, 48, 72 and 96 h. The procedure was conducted by applying a drop on the diamond plate of the ATR accessory. The measurement parameters were the same as before. Instrument control and initial data processing were performed using OPUS Software (v. 7.5, Bruker Optics, Ettlingen Germany). The FT-Raman spectra of ligands were collected on a Bruker MultiRam spectrometer (Nd:YAG laser with a CW radiation at 1064 nm) equipped with a liquid N_2 cooled germanium detector at resolution of 4 cm^{-1}, co-addition of 1024 scans, and laser power values of 300 mW. For all complexes and salts, the spectra were recorded on the Bruker dispersive Raman Spectrometer Senterra coupled with a confocal microscope with 633 nm and 532 nm lasers, lenses of different focal lengths and a sample stage with an automatic shift in the x, y, z directions; enabling in this way spectroscopic mapping of the samples with the positioning accuracy up to 0.0001 mm. The presented spectra were recorded in the range of 4450–45 cm^{-1} with a resolution of 9–18 cm^{-1} using 633 and 532 nm exciting laser lines and 25 × 1000 μm aperture, respectively.

Thermogravimetry analysis. Thermogravimetric analysis (TG) was performed on TGA 4000, PerkinElmer. Samples (mass ~5.00 mg) were measured in presence of nitrogen in the furnace atmosphere at a heating rate of 10 °C min^{-1} in the range of 25–1000 °C.

Magnetic measurements. Variable-temperature (1.8–300 K) direct current (DC) magnetic susceptibility measurements under applied field B_{DC} = 0.5 T and variable – field (0–5 T) magnetization measurements at low temperatures were carried out with Quantum Design SQUID magnetometer. Raw magnetic susceptibility data were corrected for the underlying diamagnetism and the sample holder. Magnetic measurements were carried out by crushing the crystals and restraining the sample in order to prevent any displacement due to its magnetic anisotropy.

EPR spectra. X-band EPR spectra of polycrystalline complexes were measured at 295 K using a Bruker ELEXYS E500 Spectrometer equipped with a NMR teslameter and frequency counter. The experimental spectra were simulated with the Doublet Exact ($S = 1/2$) computer program written by Dr Andrew Ozarowski from NHMFL, Florida University, Tallahassee, USA.

DFT computation. Theoretical calculations were done using the ORCA 4.0 suite of programs[56] and Gaussian 09 packet[57] without any symmetry constraints. The X-ray coordinates were used. The initial guesses were provided by calculations based on the B3LYP-D3 (ref. 58) functional in conjunction with the def2-TZVP. Calculations were performed for both "single point" and optimized molecules, as it is often done. The changes related to the density distribution on atoms and the spin distribution was small. In fact, it can be assumed that the distribution is the same. The Chemcraft[59] was employed for model preparation and visualization of the results.

Cell lines. MCF7 cell line (human breast adenocarcinoma, morphology: epithelial-like, ATCC: HTB-22), A549 cell line (human lung adenocarcinoma, morphology: epithelial, ATCC: CCL-185), human keratinocytes (HaCaT) were cultured in Dulbecco's Modified Eagle's Medium (DMEM, Corning) with phenol red, supplemented with 10% fetal bovine serum (FBS) and with 1% streptomycin/penicillin. DU-145 cell line (human prostate carcinoma); derived from metastatic site: brain and HEK293T cell line (human embryonic kidney) were cultured in minimum essential medium (MEM, Corning) with only 10% fetal bovine serum (FBS). Cultures were incubated at 37 °C under a humidified atmosphere containing 5% CO_2. Cells were passaged using a solution containing 0.05% trypsin and 0.5 mM EDTA. All media and other ingredients were purchased from ALAB, Poland.

Cytotoxic study *in vitro*. Since most of the studied compounds are insoluble in aqueous media, therefore they needed to be pre-dissolved in DMSO for biological tests. Cytotoxicity was assessed by MTT assay performed according to the protocols described previously.[51] In brief, 1 × 104 cells per well, seeded in 96-well flat bottom microtiter plate in 0.2 mL of culture medium. Cells were incubated with the complexes **1**, **3**, **4**, 2-pyridineethanol, 2-pyridinemethanol and 2-ethylpyridine compounds at various ranges of concentrations (0.01–1 mM) for 24 hours. In the first approach after that time, solutions of compounds were washed out, cells were washed three times with PBS and IC_{50} values were assessed at once (24 h). Each compound concentration was tested in five replicates and repeated at least three times. Determined values of IC_{50} (concentration of a drug required to inhibit the growth of 50% of the cells) are given as mean + SD (Standard Deviation). Furthermore, post-treatment survival assessment of the treated cells was analyzed under a fluorescence inverted microscope (Olympus IC51, Japan) with an excitation filter 470/20 nm. For this, cells were stained with two versatile fluorescence dyes: fluorescein diacetate (FDA, 5 mg mL^{-1}) and propidium iodide (PI, 5 mg mL^{-1}) in standard conditions in the dark for 20 min. Before visualization dyes were removed and cells were washed with PBS twice.

Fluorescence microscopy. Viable and dead cells were detected by staining with fluorescein diacetate (FDA, 5 mg L^{-1}) and propidium iodide (PI, 5 mg L^{-1}) for 20 min and examined using fluorescence inverted microscope (Olympus IX51, Japan) with an excitation filter of 470/20 nm. Photographs of cells after treatment with the tested compounds were taken under magnification 20×.

Cellular uptake. HEK293T, HaCat, MCF7, DU145, and A549 cells at density of 1 × 10^6 cells/2 mL were seeded on 6-well plates and were incubated with **1** and **3** (1 μM) for 24 h at standard conditions (37 °C, 5% CO_2). Additional wells were incubated with medium alone as negative control. Then, compound solutions were removed; the cells were washed twice with PBS buffer, and trypsinized. Measurement of the concentration of copper ions was carried out using a mass spectrometer (ELAN 6100 PerkinElmer) with an inductively coupled plasma (ICP-MS). For analysis collected cells were mineralized in 1 mL of 65% HNO_3 at 60 °C for 1 h. The copper content under each condition is expressed as ng mg^{-1} protein. Protein content was assessed with Bradford Protein Assay (Thermo

Scientific™).[51] The experiment was repeated at least 3 times and the results are presented as mean value + SD.

Generation of reactive oxygen species. Cellular production of reactive oxygen species (ROS) was determined by photometric tests using Cyto-ID®Hypoxia/Oxidative Stress Detection Kit (Thermo Fisher) and was carried out as described previously.[51] The assay was performed in 96-well plates, where the cells were seeded at a density of 10^5 cells per 0.2 mL of medium. The experiments were performed in darkness.

Detection of mitochondrial membrane potential (ψ). Mitochondrial membrane potential (MMP) depletion was determined by JC-10 Assay (Life Technologies, USA). DU-145 cells were seeded on 96-well plates at 1×10^4 cells per 0.2 mL. After 24 h medium was replaced with solutions of organic and inorganic compounds at IC_{50} concentration as well as gentamicin (0.5 mg mL^{-1}) and ciprofloxacin (10 μg mL^{-1}) as positive and negative control, respectively. After that, cells were incubated for 24 h at standard condition (37 °C, 5% CO_2). Then, they were washed twice with PBS buffer and incubated with JC-10 for 1 hour. Afterwards, emission was measured at two different excitation wavelengths ($\lambda_{ex} = 540$ nm, $\lambda_{em} = 570$ nm) and ($\lambda_{ex} = 485$ nm, $\lambda_{em} = 530$ nm). Results are presented as the intensity ratio of red to green emission (mean + SD).

Author contributions

M. M.: study conception and design, administrative support, data collection and/or assembly, FT-IR, Raman and TGA data analysis and interpretation, and manuscript writing. A. Ś., B. M.: X-ray measurements and data analysis for crystals. U. K., S. K., A. K.: biological data analysis, data interpretation, and methodology development. A. B.: magnetic measurements, EPR study, data analysis and interpretation, and final approval of the manuscript, D. B.: theoretical computation, manuscript writing and graphical abstract preparation. T. M.: data collection. All authors have read and agreed to the published version of the manuscript.

Conflicts of interest

There are no conflicts to declare.

Acknowledgements

The work was financially supported by a statutory activity subsidy from the Polish Ministry of Science and Higher Education for the Faculty of Chemistry, Wroclaw University of Science and Technology. The work was supported by the National Science Centre, Poland, under research project "Hydroxyl pyridine derivatives as ligands in Co(II) and Cu(II) complexes of biological and application significance", 2021/05/X/ST4/00312A. The UV-Vis measurements were carried out with the equipment purchased thanks to the financial support of the Polish National Science Centre (Grant 2016/23/D/ST5/00269). Biological study was partially funded by the Polish National Science Centre (grant number 2020/37/N/ST4/02698). The generous computer time from the Wroclaw Supercomputer and Networking Center is acknowledged.

Notes and references

1 V. T. Yilmaz, S. Hamamci and C. Thone, *Polyhedron*, 2004, **23**, 841–848.
2 N. Lah and I. Leban, *Struct. Chem.*, 2010, **21**, 263–267.
3 S.-C. Cheng and H.-H. Wei, *Inorg. Chim. Acta*, 2002, **340**, 105–113.
4 W. E. Marsh, W. E. Hatfield and D. J. Hodgson, *Inorg. Chem.*, 1982, **21**, 2679–2684.
5 N. Lah, I. Leban and R. Clérac, *Eur. J. Inorg. Chem.*, 2006, 4888–4894.
6 M. Zienkiewicz-Machnik, J. Masternak, K. Kazimierczuk and B. Barszcz, *J. Mol. Struct.*, 2016, **1126**, 37–46.
7 S. M. Mobin and A. Mohammad, *Dalton Trans.*, 2014, **43**, 13032–13040.
8 O. Zeghouan, M. A. Dems, S. Sellami, H. Merazig and J. C. Daran, *Acta Crystallogr., Sect. E: Crystallogr. Commun.*, 2018, **E74**, 1042–1048.
9 E. Sayın, G. S. Kürkçüoğlu, O. Z. Yeşilel and M. Taş, *J. Coord. Chem.*, 2016, **69**, 1226–1235.
10 M. C. Biagini, M. Ferrari, M. Lanfranchi, L. Marchiò and M. A. Pellinghelli, *J. Chem. Soc., Dalton Trans.*, 1999, 1575–1580.
11 H. Amouri and M. Gruselle, *Chirality in Transition Metal Chemistry: Molecules, Supramolecular Assemblies and Materials*, Wiley, Chichester, U.K, 2008.
12 P. Calamai, S. Carotti, A. Guerri, L. Messori, E. Mini, P. Orioli and G. P. J. Speroni, *Inorg. Biochem.*, 1997, **66**, 103–109.
13 C. Icsel, V. T. Yilmaz, F. Ari, E. Ulukaya and W. T. Harrison, *Eur. J. Med. Chem.*, 2013, **60**, 386–394.
14 A. Jabłońska-Wawrzycka, B. Barszcz, M. Zienkiewicz, M. Hodorowicz, J. Jezierska, K. Stadnicka, Ł. Lechowicz and W. Kaca, *Spectrochim. Acta, Part A*, 2014, **129**, 632–642.
15 N. Aztopal, D. Karakas, B. Cevatemre, F. Ari, C. Icsel, M. G. Daidone and E. Ulukaya, *Bioorg. Med. Chem.*, 2017, **25**, 269–276.
16 (*a*) M. Malik, D. C. Bienko, U. K. Komornicka, A. Kyzioł, M. Dryś, A. Świtlicka, E. Dyguda-Kazimierowicz and W. Jedwabny, *J. Inorg. Biochem.*, 2021, **215**, 111311; (*b*) B. Morzyk-Ociepa, K. Szmigiel-Bakalarz, M. Nentwig, O. Oeckler, M. Malik-Gajewska, E. Turlej, J. Wietrzyk and D. Michalska, *Inorg. Chim. Acta*, 2019, **490**, 68–77; (*c*) B. Morzyk-Ociepa, K. Szmigiel, I. Turowska-Tyrk, M. Malik-Gajewska, J. Banach and J. Wietrzyk, *Polyhedron*, 2018, **153**, 88–98; (*d*) S. S. Massoud, F. R. Louka, M. A. Al-Hasan, R. Vicente and F. A. Mautner, *New J. Chem.*, 2015, **39**, 5944–5952; (*e*) F. Hasanvand, R. A. Ahmadi and S. Amani, *J. Sci., Islamic Repub. Iran*, 2012, **23**, 37–43; (*f*) J. Masternak, M. Zienkiewicz-Machnik, I. Łakomska, M. Hodorowicz, K. Kazimierczuk, M. Nosek, A. Majkowska-Młynarczyk, J. Wietrzyk and B. Barszcz, *Int. J. Mol. Sci.*, 2021, **22**, 7286–7313.
17 W. Choong and N. C. Stephenson, *Cryst. Struct. Commun.*, 1975, **4**, 275–280.

18 A. Okuniewski, D. Rosiak, J. Chojnacki and B. Becker, *Polyhedron*, 2015, **90**, 47–57.
19 M. Llunell, D. Casanova, J. Cirera, P. Alemany and S. Alvarez, *SHAPE version 2.0*., Universitat de Barcelona, 2010.
20 F. F. Awwadi, M. M. Turnbull, M. I. Alwahsh and S. F. Haddad, *New J. Chem.*, 2018, **42**, 10642–10650.
21 C. Villa-Perez, I. C. Ortega, A. Velez-Macias, A. M. Payan, G. A. Echeverrıa, D. B. Soria and G. C. Valencia-Uribe, *New J. Chem.*, 2018, **42**, 7166–7176.
22 F. Awwadi, R. D. Willett and B. Twamley, *Cryst. Growth Des.*, 2011, **11**, 5316–5323.
23 A. Amoedo-Portela, R. Carballo, J. S. Casas, E. Garcia-Martinez, A. B. Lago-Blanco, A. Sanchez-Gonzalez, J. Sordo and E. M. Vazquez-Lopez, *Z. Anorg. Allg. Chem.*, 2005, **631**, 2241–2246.
24 C. F. Macrae, I. J. Bruno, J. A. Chisholm, P. R. Edfinfton, P. McCabe, E. Pidcock, L. Rodriguez-Monge, R. Taylor, J. van de Streek and P. A. Wood, *J. Appl. Crystallogr.*, 2008, **41**, 466–470.
25 A. W. Addison, T. N. Rao, J. Reedijk, J. Rijn and G. C. Verschoor, *J. Chem. Soc., Dalton Trans.*, 1984, 1349–1356.
26 S. Kashyap, U. P. Singh, A. K. Singh, P. Kumar and S. Pratap Singh, *Transition Met. Chem.*, 2013, **38**, 573–585.
27 N. S. Gill and M. Sterns, *Inorg. Chem.*, 1970, **9**, 1619–1625.
28 J. Cirera, P. Alemany and S. Alvarez, *Chem.–Eur. J.*, 2004, **10**, 190–207.
29 D. Casanova, J. Cirera, M. Llunell, P. Alemany, D. Avnir and S. Alvarez, *J. Am. Chem. Soc.*, 2004, **126**, 1755–1763.
30 B. Antonioli, D. J. Bray, J. K. Clegg, K. A. Jolliffe, K. Gloe, K. Gloe and L. F. Lindoy, *Polyhedron*, 2007, **26**, 673–678.
31 R. Dennington; T. A. Keith and J. M. Millam, *GaussView, Version 6*, Semichem Inc., Shawnee Mission, KS, (2016.
32 K. Nakamoto, *Infrared and Raman Spectra of Inorganic and Coordination Compounds, Part B*, J. Wiley & Sons Inc., New York, 2009.
33 N. F. Chilton, R. P. Anderson, L. D. Turner, A. Soncini and K. S. Murray, *J. Comput. Chem.*, 2013, **34**, 1164–1175.
34 O. Kahn, *Molecular Magnetism*, VCH, New York, 1993.
35 W. E. Marsh, K. C. Patel, W. E. Hatfield and D. J. Hodgson, *Inorg. Chem.*, 1983, **22**, 511–515.
36 V. H. Crawford, H. W. Richardson, J. /R. Wasson, D. J. Hodgson and W. E. Hatfield, , *Inorg. Chem.*, 1976, **15**, 2107–2110.
37 B. Graham, M. T. W. Hearn, P. C. Junk, C. M. Kepert, F. E. Mabbs, B. Moubaraki, K. S. Murray and L. Spiccia, *Inorg. Chem.*, 2001, **40**, 1536–1543.
38 K. Skorda, T. C. Stamatatos, A. P. Vafiadis, A. T. Lithoxoidou, A. Terzis, S. P. Perlepes, J. Mroziński, C. P. Raptopoulou, J. C. Plakatouras and E. G. Bakalbassis, *Inorg. Chim. Acta*, 2005, **358**, 565–582.
39 S. Thakurta, P. Roy, G. Rosair, C. J. Gómez-García, E. Garribba and S. Mitra, *Polyhedron*, 2009, **28**, 695–702.
40 M. Grove, J. Sletten, M. Julve and F. Floret, *J. Chem. Soc., Dalton Trans.*, 2001, 2487–2493.
41 M. Barwiolek, A. Kaczmarek-Kędziera, T. M. Muzioł, D. Jankowska, J. Jezierska and A. Bieńko, *Int. J. Mol. Sci.*, 2020, **21**, 4587.
42 B. Kozlevčar and P. Šegedin, *Croat. Chem. Acta*, 2008, **81**, 369–379.
43 Ch. Chow, K. Chang and R. D. Willett, *J. Chem. Phys.*, 1973, **59**, 2629.
44 P. Kołoczek, A. Skórska-Stania, A. Cierniak, V. Sebastian, U. K. Komarnicka, M. Płotek and A. Kyzioł, *Eur. J. Pharm. Biopharm.*, 2018, **128**, 69–81.
45 W. Zhang, Y. Shi, Y. Chen, J. Hao, X. Sha and X. Fang, *Biomaterials*, 2011, **32**, 5934–5943.
46 National Cancer Institute, posted to the SEER website, *SEER Cancer Statistics Review 1975–2018*, ed. N. Howlader, A. M. Noone, M. Krapcho, et al., 2021, last accessed 19 April 2021.
47 A. Kellett, O. Howe, M. O'Connor, M. McCann, B. S. Creaven, S. McClean, A. Foltyn-Arfa Kia, A. Casey and M. Devereux, *Free Radic. Biol. Med.*, 2012, **53**, 564–576.
48 E. Budzisz, M. Miernicka, I. P. Lorenz, P. Mayer, U. Krajewska and M. Rozalski, *Polyhedron*, 2009, **28**, 637–645.
49 (*a*) S. Gama, F. Mendes, F. Marques, I. C. Santos, M. Fernanda Carvalho, I. Correia, J. C. Pessoa, I. Santos and A. Paulo, *J. Inorg. Biochem.*, 2011, **105**, 637–644; (*b*) C. Santini, M. Pellei, V. Gandin, M. Porchia, F. Tisato and C. Marzano, *Chem. Rev.*, 2014, **114**, 815–862; (*c*) C. Molinaro, A. Martoriati, L. Pelinski and K. Cailliau, *Cancers*, 2020, **12**, 2863–2890.
50 A. Kyzioł, A. Cierniak, J. Gubernator, A. Markowski, M. Jeżowska-Bojczuk and U. K. Komarnicka, *Dalton Trans.*, 2018, **47**, 1981–1992.
51 S. Kozieł, U. K. Komarnicka, A. Ziółkowska, A. Skórska-Stania, B. Pucelik, M. Płotek, V. Sebastian, A. Bieńko, G. Stochel and A. Kyzioł, *Inorg. Chem. Front.*, 2020, **7**, 3386–3401.
52 Q. Zhai, H. Ji, Z. Zheng, X. Yu, L. Sun and X. Liu, *J. Cell. Physiol.*, 2000, **184**, 161–170.
53 H. Yang, R. M. Villani, H. Wang, M. J. Simpson, M. S. Roberts, M. Tang and X. Liang, *J. Exp. Clin. Cancer Res.*, 2018, **37**, 266–275.
54 C. Guo, L. Sun, X. Chen and D. Zhang, *Neural Regener. Res.*, 2013, **8**, 2003–2014.
55 G. M. Sheldrick, Crystal structure refinement with SHELXL, *Acta Crystallogr., Sect. C: Struct. Chem.*, 2015, **71**, 3–8.
56 F. Neese, *Software update: the ORCA program system, version 4.0*, WIREs Comput Mol Sci, 2018, 8, p. 1327.
57 M. J. Frisch, G. W. Trucks, H. B. Schlegel, G. E. Scuseria, M. A. Robb, J. R. Cheeseman, G. Scalmani, V. Barone, B. Mennucci, G. A. Petersson, H. Nakatsuji, M. Caricato, X. Li, H. P. Hratchian, A. F. Izmaylov, J. Bloino, G. Zheng, J. L. Sonnenberg, M. Hada, M. Ehara, K. Toyota, R. Fukuda, J. Hasegawa, M. Ishida, T. Nakajima, Y. Honda, O. Kitao, H. Nakai, T. Vreven, J. A. Montgomery Jr., J. E. Peralta, F. Ogliaro, M. Bearpark, J. J. Heyd, E. Brothers, K. N. Kudin, V. N. Staroverov, R. Kobayashi, J. Normand, K. Raghavachari, A. Rendell, J. C. Burant, S. S. Iyengar, J. Tomasi, M. Cossi, N. Rega, J. M. Millam,

M. Klene, J. E. Knox, J. B. Cross, V. Bakken, C. Adamo, J. Jaramillo, R. Gomperts, R. E. Stratmann, O. Yazyev, A. J. Austin, R. Cammi, C. Pomelli, J. W. Ochterski, R. L. Martin, K. Morokuma, V. G. Zakrzewski, G. A. Voth, P. Salvador, J. J. Dannenberg, S. Dapprich, A. D. Daniels, Ö. Farkas, J. B. Foresman, J. V. Ortiz, J. Cioslowski and D. J. Fox, Wallingford CT, 2009.

58 S. Grimme, J. Antony, S. Ehrlich and H. Krieg, *J. Chem. Phys.*, 2010, **132**, 154104.

59 *Chemcraft – graphical software for visualization of quantum chemistry computations* **https://www.chemcraftprog.com**.